Catalyst Development for Electrochemical Water Splitting

By

Tess Seuferling

Submitted to the graduate degree program in the Department of Chemical and Petroleum Engineering and the Graduate Faculty of the University of Kansas in partial fulfillment of the requirements for the degree of Master of Science in Chemical Engineering.

Committee Members

Prof. Kevin C. Leonard, Chair

Prof. Prajnaparamita Dhar

Prof. Raghunath V. Chaudhari

August 21, 2019

Date Defended

The Dissertation Committee for Tess Seuferling certifies that this is the approved version of the following dissertation: Catalyst Development for Electrochemical Water Splitting

---

Prof. Kevin C. Leonard, Chair

Date Approved

Abstract

The world population is growing at a rate untenable for our current energy resources to keep up with. This combined with the factors of depleting nonrenewable energy sources, i.e. fossil fuels, and environmental impacts of obtaining and utilizing these resources has created an urgent demand for new alternative clean energy sources. Hydrogen has shown promise as a potential fuel to help alleviate the use of these destructive energy sources. The use of hydrogen in a fuel cell cars is rated as a zero emissions fuel. However, a challenge associated with using hydrogen is the current means of production. Today, almost all hydrogen is produced through steam reformation, at high temperatures and pressures requiring excess energy, and which also produces carbon dioxide. The emissions of carbon dioxide at the production step essentially offsets the zero emissions at the tailpipe. Water electrolysis has been at the forefront to address this concern. Previously this technique was not commercially viable due to costly materials and operational requirements. With recent advancements in research this technology is becoming increasingly feasible.

To continue to improve this process and lower costs, a main factor is the development of electrocatalysts for the hydrogen evolution reaction (HER) and oxygen evolution reaction (OER) in splitting water. It has been particularly difficult to balance an active electrocatalyst with operation conditions. Typically, these catalysts were comprised of expensive, rare metals that would not be practical for large scale production. For the HER, platinum is the leading catalyst in acid. Acidic conditions with the abundance of protons is preferred for the HER. Unfortunately, this is hard to implement due to the corrosive nature of acids and scarcity of platinum. OER on the other hand is suited for alkaline conditions. The OER is also especially complicated due to the four electron/four proton transfer reaction. For these reasons, the OER in alkaline conditions is where this thesis commenced.

The purpose of this thesis is to search for a reasonably priced and accessible electrocatalyst for both the OER and HER that is highly active and porous in structure. Utilizing a microwave-assisted synthesis technique, electrocatalysts comprised of FeNi for OER and $Co_{0.8}$:$Ni_{0.2}$ for HER resulted in the lowest overpotentials. These low overpotentials mean the reactions are closer to thermodynamic equilibrium potentials and would require less electricity to split the water. With this electrocatalyst, the next goal is to further improve performance by fabricating an electrode with a 3D, porous, high surface area in order to increase mass transfer to the active sites. This was accomplished by using a nickel foam support for both OER and HER. Finally by adjusting the electrolytic solution from 1 M NaOH to 3 M NaOH we were able to complete OER using an FeNi and HER using $Co_{0.8}$:$Ni_{0.2}$ nanoamorpohous electrocatalysts electrophoretically deposited on nickel foam to reach overpotentials of 194 mV and 120 mV respectively at 10 mA cm^{-2}. Ultimately, if fueled by renewable electricity such as wind, solar, hydroelectric, and with the use of highly active electrocatalysts the widespread implementation of water electrolysis could be in the near future.

Acknowledgments

There are moments where a split decision can shape your life to where it becomes unimaginable any other way. For me, attending an American Institute of Chemical Engineers meeting freshman year during undergrad at the University of Kansas was that decision. And full disclosure it was for the free pizza. However, that seemingly minor decision to attend and then to approach the speaker after led me to my advisor, Dr. Kevin Leonard. And Kevin is a whiz. Not only is he brilliant, but his ability to educate is unparalleled. In the midst of today's subpar professors, Kevin is unique in his ability to maintain a research lab with a healthy work-life balance and great innovation while also inspiring students through his courses. I was fortunate to have found this rare combination of willingness and enthusiasm to help me learn in an advisor which made my Master's experience exceptional. Throughout my time working with Kevin, he has shared a wealth of wisdom from electrochemistry to ornithology. I am eternally grateful to have met and to call Kevin a friend.

I am also incredibly thankful for all my wonderful labmates during my time in the Leonard Lab. From the very first, Kelly Song who co-founded the beginnings of this research and is one of the funniest people I know. To all the grad students, a truly great group of guys: Tim McDonald, Joe Barforoush, Charles Shaughnessy, Dylan Jantz, and Matt Stalcup. Lastly to the numerous undergrads, there have been many and they made the lab an entertaining place to work. Special mention goes out to Libby Brungardt, the liveliest of the bunch.

To all the people over the last two years that helped me to achieve a Master's, something I never thought I would do. My close friend, Kayley Perkins, for her endless inspirational quotes and support. My fellow classmates Anoop, Faiz, Simon, and Kyle. Additionally, I must extend a huge thank you to everyone at the CEBC. From the staff to permanent researchers to other fellow graduate students, they make this facility an amazing place to be. Many, many thanks goes to

Ed Atchison who is invaluable at the CEBC for coming up with solutions to any of your research design problems and who is an outstanding coworker. And I am appreciative to Dr. Chaudhari and Dr. Dhar for serving on my thesis committee and for their extended support.

Finally there are no particular words that can encompass the gratitude I would like to express to my family, so I'll keep it short and sweet. Thanks to my sister, Marci, and the furry queen Jesa. Thank you to my parents, Marianne and Dale, for this life. Marianne for her unlimited support over the years. And to Dale, for everything but not limited to providing adventures and endless opportunities, inspiring quite success, and for being a groovy father and undoubtedly the best human out there.

Contents

List of Figures

Chapter 1

Introduction

1.1 Global Energy Status

One of the top challenges facing the world today is implementing sustainable energy resources. The global population is growing at a rate untenable for the current fuel sources. Additionally, the nonrenewable energy resources employed today are negatively impacting the earth at an unsustainable rate. Lastly, an important consideration is the discrepancy of accessible energy resource leading to energy poor regions. Nearly a decade ago, at the Clean Industrial Revolution event, United Nations Secretary-General Ban Ki Moon, amid discussing these issues, eloquently put "..we cannot burn our way to prosperity." [2] To address these concerns it is important to consider why they are tough to solve.

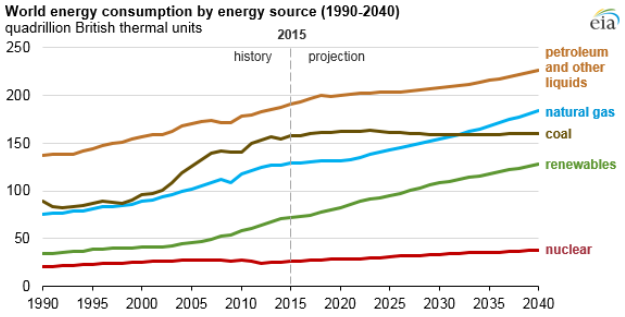

Figure 1.1. Chronological growth of global energy consumption tabulated by energy supply resource. [1]

Over 70% of the energy consumed globally is classified as fossil fuels e.g. liquids, natural gas, and coal. However, these fuels are produced in processes that have had years to be cultivated. It takes time and resources to make a process efficient enough to replace these established fuel sources. Consider this combined with the increasing demand for energy as seen in Figure 1.1 as well as the inherent properties that make fossil fuels useful such as their high energy density and ability to transport and store easily. These factors have dissuaded research into alternative fuels.

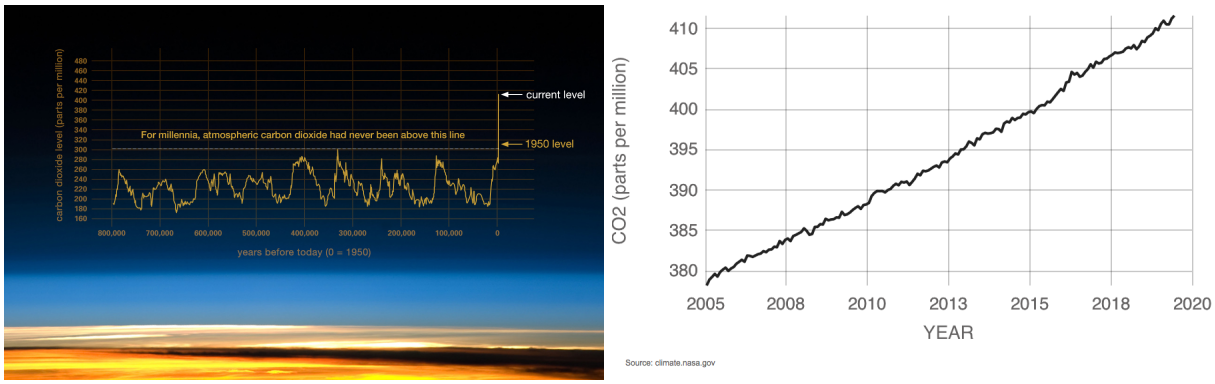

(a) Levels of global carbon dioxide over 800,000 years up until 1950.[3]

(b) Dramatic increase of carbon dioxide levels in the atmosphere over the last six decades.[4]

Figure 1.2. Carbon Dioxide level comparison

However, over the last few decades two important factors have motivated alternative fuel solutions. First is the vastly disproportionate rate at which fossil fuels are generated and consumed. Also with the increased demand, fossil fuels will be depleted within a matter of mere decades. Second is the environmental impacts burning fossil fuels has on the environment. Greenhouse gases, namely carbon dioxide, is produced by burning these fuels. Carbon dioxide is particularly impactful due to its abundance, slow decomposition rate, and capacity to trap heat in the atmosphere.[5] Shown in 1.2a is the levels of carbon dioxide over the past 800,000 years while 1.2b is the building rate of concentration of carbon dioxide in earth's atmosphere over just the last six decades. The increase is unprecedented and must be addressed in order to avoid inhabitable conditions. There are two main courses of action to remedy this issue: decrease the amount produced and capture the remaining emitted carbon dioxide to use in other fuel applications.[3]

All these concerns amount to the need for an alternative fuel source with the following criteria: renewable, low emissions for a full lifecycle analysis, efficient and vast enough to meet the growing energy demands as well as widely available to all regions of the world. This will be achieved by using a combination of energy sources. Hydrogen has been proposed as a viable option for one of these energy sources.

1.2 Hydrogen Prospects

Hydrogen demand is projected to increase with its consumption in a variety of markets such as oil refining and multiple chemical production processes like ammonia and methanol.[6] Moreover, hydrogen generation is expected to rise with growing interest in green energy and stricter government regulations on emissions. In particular hydrogen can be used for its energy storing capabilities to reduce dependence on fossil fuels and decrease emissions as a clean burning fuel.[7,8] However, the leading method for producing hydrogen is through steam reformation with substantial carbon dioxide emissions. A complete lifecycle of the process must be considered and the current method negates the use of hydrogen as an environmentally alternative when the mode of production produces near equivalent emissions as burning fossil fuels.[9,10] The environmental concerns combined with the climbing global demand has pushed for market diversity and new production methods for hydrogen. The method gaining the most momentum for producing hydrogen is water electrolysis or water splitting.[7]

1.3 Water Electrolysis

There are three main avenues for water splitting categorized by the energy source to fuel the reaction: electrolysis (electricity), thermolysis (heat), and photolysis (solar).[11] Water electrolysis has become a serious contender to replace current CO_2 generating methods for producing hydrogen. In electrolysis, an electrical current is passed through water where the energy changes to chemical at an electrode-solution interface by a charge transfer reaction. Simply put: water electrolysis splits water into oxygen and hydrogen. Thereby the only by-product is oxygen, and can be considered a zero emissions proceess.[11] The overall governing equation is:

$$2H_2O \longrightarrow 2H_2 + O_2 \tag{1.1}$$

Not simply put is the amount of energy required to obtain hydrogen. This reaction has a large Gibbs free energy change of $\Delta\ G^0 = +237$ kJ/mol.[12,13] Through the Nernst equation this equates to $E^0 = 1.23$ V.[14] The current electricity demand for water electrolysis would strain the grid and again lessen the positive impact on the environment. An alternative to grid electricity would be to

utilize other renewable resources recently improved such as wind, solar, hydroelectric, biomass, and geothermal. Another advantage is geographically at least one of these sources would be an option to augment water electrolysis.[11]

Some of the grand challenges facing scientists today is lowering the energy barrier to split water, store the hydrogen, lower the cost of specialty materials to achieve this process, scale up production, and overall fundamental research insights at each step.[15] This work will attempt to address the first challenge of lowering the energy requirement to split water by the use of an electrocatalyst. More specifically, the electrocatalysts will be tested for an alkaline electrolyzer meaning the catalyst must perform well in basic conditions.

1.4 Electrochemistry Background

The primary technique used to evaluate the performance of the electrocatalysts developed in this work was cyclic voltammetry. The experimental set up for these tests were a three electrode system: working, counter, and reference. In the cyclic voltammetry tests, the potential applied to the working electrode was cycled while measuring the resultant current. The performance was evaluated based on two factors: the onset potential and the current density magnitude at 10 mA cm^{-2}. The onset potential reflects the minimum amount of energy required for the reaction to take place. This is where the current begins to increase from zero. The current density can be directly related to the amount of product produced. Seen in Equations 1.2 and 1.7 which are the reactions occurring at the electrodes, the measurement of electrons transferring corresponds to the rate of oxygen and hydrogen produced. Additionally, the cyclic voltammogram gives information on reversibility as well as kinetic and mass transfer limitations. If the reaction is reversible, the scan forward, from low potential to high, will overlap with the backward scan, high potential to low. A gap between the scans is evidence of surface changes or capacitance charging. For this research most all cyclic voltammograms indicate kinetic limitations. If the system is mass transfer limited, the cyclic voltammogram will display a plateau as the potential is increased.

1.5 Electrocatalyst Development for the Oxygen Evolution Reaction (OER)

In water electrolysis, the oxygen evolution reaction (OER) is as follows:

$$4\mathrm{OH}^- \rightleftharpoons 2\mathrm{H_2O} + \mathrm{O_2} + 4\,\mathrm{e}^- \tag{1.2}$$

Within the electrolyzer, the OER takes place at the anode where oxygen is produced. Cost, availability, and activity are all factors equally important in electrocatalyst design. Initial studies into active electrocatalysts yielded optimal results when using rare, costly metal oxides IrO_2 and RuO_2 in acidic media.[16–19] According to recent published studies on OER electrocatalysts, transition metal oxides have shown encouraging results. These transition metals included Fe, Ni, Co, Mn, Mo, and W and were in alkaline media.[20–22]

The OER is the half reaction that limits the overall water splitting efficiency, due to the complexity of the four-proton/four electron transfer. While there is no definitive mechanism for the OER, the most commonly accepted mechanism in alkaline media in equations (1.3) – (1.6).[23]

$$S + OH^- \rightleftharpoons S - OH + e^- \tag{1.3}$$

$$S - OH + OH^- \rightleftharpoons S - O + H_2O + e^- \tag{1.4}$$

$$S - O + OH^- \rightleftharpoons S - OOH + e^- \tag{1.5}$$

$$S - OOH + OH^- \rightleftharpoons S + O_2 + H_2O + e^- \tag{1.6}$$

Currently no catalyst can perform the OER at thermodynamic potentials. This is due to the linear-scaling relationship between adsorbed OH ($\cdot$OH) and adsorbed OOH ($\cdot$OOH). Rossmeisl and co-workers performed density functional theory (DFT) calculations on a wide range of OER catalysts and found that as the binding strength of $\cdot$OH weakens, the binding strength of $\cdot$OOH

weakens linearly.[24] Figure 1.3 shows the linear scaling relationship between the adsorption energy of $\cdot$OOH, ΔE_{OOH}, and the adsorption energy of $\cdot$OH, ΔE_{OH}, for several types of catalysts. As can be seen by the mechanism, one would want to break this scaling relationship to have the optimum binding energy for each catalyst. The red star on Figure 1.3 represents the binding energies for a thermodynamically ideal catalyst. Rossmeisl concluded that this scaling relation provides a lower limit of the OER overpotential of ca. 0.2 - 0.4 V overpotential.[23,24]

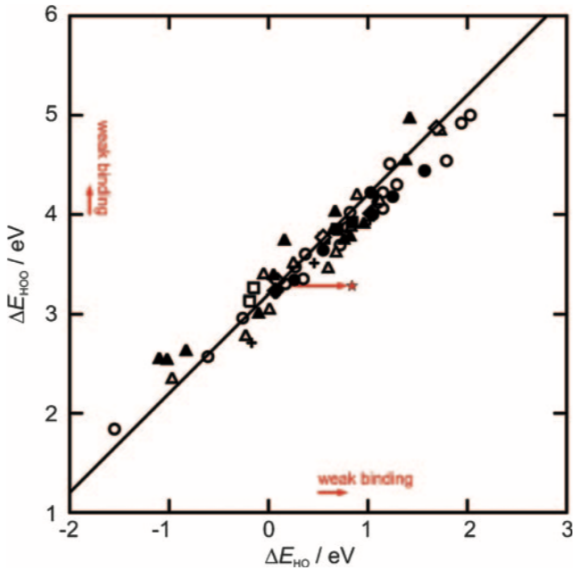

Figure 1.3. Adsorption energy of OOH vs. adsorption energy of OH for perovskites (circle), rutiles (triangle), anatase (diamond), Mn_xO_y (square), Co_3O_4 (plus sign), and NiO oxides, based on density functional theory (DFT) calculations. The hollow symbols represent adsorption energies for clean surfaces, and the solid shapes represent adsorption energies for surfaces with high coverage. The red star indicates the adsorption energies of an ideal OER catalyst.[24]

In order to try to achieve this minimum possible overpotential, researchers have been investigating catalysts comprised of multiple metals. Among the most active OER catalysts, NiFe-based materials have achieved some of the lowest overpotentials reported for the OER, outperforming Ir and Ru-based electrocatalysts.[25–29] One of the first reports of NiFe-based catalysts was when Edison and Junger found that the Fe impurities in Ni-based alkaline batteries electrodes decreased capacity and cycle life. Additional studies revealed that Fe impurities in Ni would lower the OER overpotential.[25] A major area of research has been to improve the activity of NiFe-based alkaline OER catalysts.[25] It has been shown that both the morphology and the ratio of nickel-to-iron has been shown to govern OER activity. The optimum elemental ratio has been found to be ca. 80%

Ni and ca. 20% Fe where Fe content above ca. 25% results in segregation of the metals, leading to low active site densities.[29,30] Recently, numerous reports of the layered double hydroxide (LDH) class of NiFe materials as OER catalysts have emerged. LDHs are 2-D layered materials that have high activity, but are not amenable to creating highly porous 3D structures.

1.6 Electrocatalyst Development for the Hydrogen Evolution Reaction (HER)

The favored condition for HER is typically in acid where there is a single product and no side reactions.[31,32] However, with OER constraints it is easier to adapt HER in alkaline than OER in acid. Within an alkaline water electrolyzer, the hydrogen evolution reaction (HER) occurs at the cathode with the predominant reaction being water reduction. This is shown by the following:

$$2\mathrm{H_2O} + 2\mathrm{e^-} \rightleftharpoons \mathrm{H_2} + 2\mathrm{OH^-} \tag{1.7}$$

The mechanism for the HER in alkaline media is similar to the mechanism in acidic media and is shown in equations (1.8) – (1.10).

$$S + \mathrm{H_2O} + e^- \rightleftharpoons S - H_{ads} + \mathrm{OH^-} \tag{1.8}$$

$$S - H_{ads} + S - H_{ads} \rightleftharpoons 2S + \mathrm{H_2} \tag{1.9}$$

or

$$S - H_{ads} + \mathrm{H_2O} + e^- \rightleftharpoons S + \mathrm{H_2} + \mathrm{OH^-} \tag{1.10}$$

Contrary to the OER mechanism, the HER mechanism mainly depends on the adsorption strength of H on the surface of the catalysts. For the HER, most studies have shown platinum to be the prominent electrocatalyst. This can be seen in the volcano plot Figure 1.4. In this plot, the HER activity is plotted against the free energy associated with adsorption of the hydrogen atom.

At the top of the volcano is where the associated binding energy is optimal, meaning not too strong or weak.[33] Also an important note for Figure 1.4 is that the elements located closest to the peak of the volcano are all rare and expensive. Recent thought is that by combining certain lower elements in specific quantities could achieve similar results to platinum. Thus, it is important to find new catalysts that can have the same performance as Pt, but are comprised of non-precious metals.

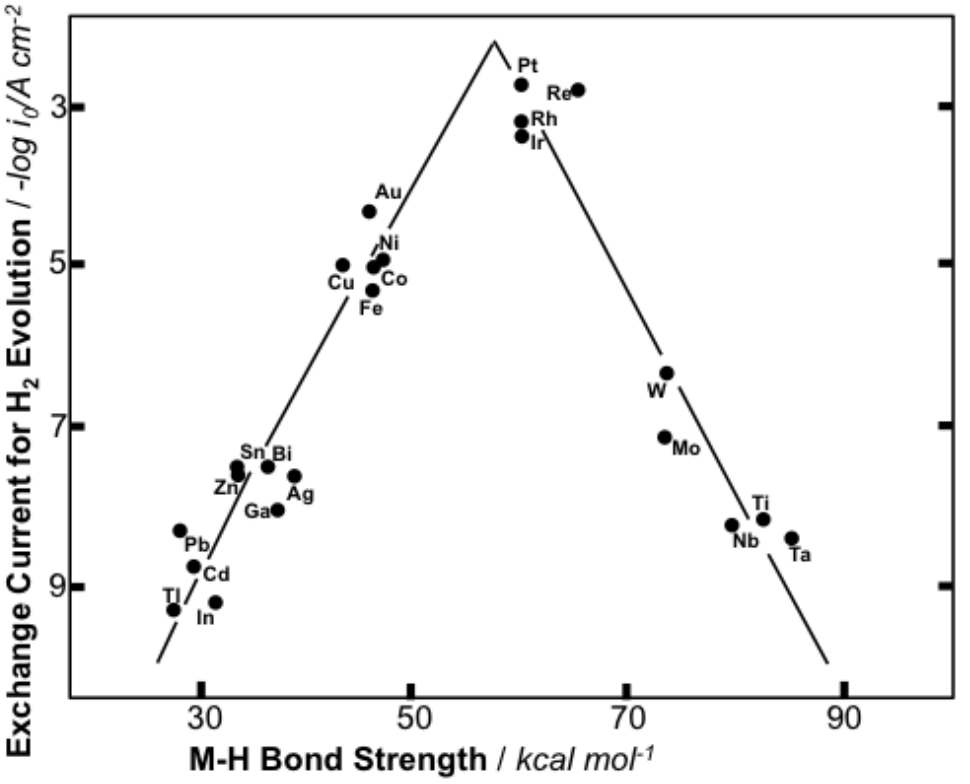

Figure 1.4. Volcano plot of elemental catalytic activity for the hydrogen evolution reaction.[33]

1.7 Overall Electrocatalyst Development

Unfortunately, water electrolysis has some major problems which have prevented large scale production of hydrogen.[34] The main questions that need to be answered are in the following:

1. How will the synergistic effects of the multimetal catalysts effect performance and can they achieve a higher performance than current champion noble metals?

2. Is it possible to create 3D porous structures of highly active catalysts to increase active site densities and promote mass-transfer to and from the electrode surface?

This thesis details efforts to answer these fundamental problems. Chapter 2 of this work compares a crystalline structure to a nanoamorphous nanoparticle structure morphology in addition to deposition techniques at optimal conditions. The details of the synthesis method developed to create a nanoamorphous nanoparticle structure electrodeposited evenly onto a flat support are included in this second chapter. In Chapter 3 and Chapter 4, are complimentary studies conducted to determine optimal electrocatalyst compositions for OER and HER respectively using the developed synthesis method in Chapter 2. Additionally in these chapters, improvements were made to process conditions by increasing molarity of the alkaline solution from 1 M to 3 M NaOH to more closely reflect industry conditions as well as provide additional hydroxide ions. Also in order to promote reaction activity, high surface area supports like carbon fiber paper and nickel foam were evaluated for substrate possibilities.

Chapter 2

Materials Development and Characterization[1]

2.1 Introduction

The development of efficient, earth-abundant electrocatalysts for the oxygen evolution reaction (OER) is of great importance to solar fuel production, because the OER is the half reaction that limits the overall efficiency.[35–37] Developing catalysts for the OER is especially challenging since the oxidation of water to oxygen occurs through a complex four-electron/four-proton transfer[24] and many materials require a significant overpotential to drive the catalysis.[38] Traditionally, the best catalysts for the OER have been composed of the noble metals Ru and Ir.[17,39,40] However, since the discovery that iron impurities can improve the OER activity of nickel oxide electrocatalysts,[40,41] nickel–iron oxyhydroxides $Ni_{1-x}Fe_xOOH$, specifically the layered double hydroxide (LDH) structure of $Ni_{1-x}Fe_xOOH$, have emerged as promising non- precious metal OER electrocatalysts in alkaline media and can rival the performance of iridium oxides.[42–60]

Experimental analysis of nickel to iron ratios has shown that approximately a $Fe_{0.2}$:$Ni_{0.8}$ ratio provides optimum catalytic performance.[27,44,53,61–64] This optimum ratio has been supported by a recent study by Bell and co-workers, which coupled X-ray absorption spectroscopy (XAS) with density functional theory (DFT) calculations.[65] This study showed that if the Fe levels rise above ca. 25%, segregation occurs and an inactive g- FeOOH phase is formed.[65] In addition, DFT

[1]This section has been adapted from published article.[29]

calculations from this study showed that the isolated iron sites within the $Ni_{1-x}Fe_xOOH$ matrix are highly active for the OER, while Ni sites in the $Ni_{1-x}Fe_xOOH$ matrix are not active for the oxidation of water.[65] The existence of "fast" Fe sites and "slow" Ni sites in $Ni_{1-x}Fe_xOOH$ was recently verified experimentally by Bard and co-workers.[66] The Bard study used the surface interrogation mode of scanning electrochemical microscopy (SI-SECM) to probe the kinetics of the active sites on iron, nickel, and nickel– iron (oxy)hydroxides.[66] It is known that insights into the intrinsic activity of a catalyst can be obtained via SI-SECM, which measures the active site density and the kinetic rate constants of catalyst sites via an electrochemical titration.[67–70] In Bard's study, they observed that two types of catalytic sites existed for $Ni_{0.8}Fe_{0.2}OOH$; "fast" sites with a kinetic rate constant of 1.70 s^{-1} per site and "slow" sites with a kinetic rate constant of 0.056 s^{-1} per site.[66] Bard also showed that the percentage of "fast" sites matched well with the iron atom content in the $Ni_{0.8}Fe_{0.2}OOH$ matrix, providing further experimental evidence for the existence of both "fast" and "slow" sites in $Ni_{1-x}Fe_xOOH$. However, this finding implies that only 20% of the catalytic surface is highly active, and it may be possible to further improve the OER performance of nickel–iron electrocatalysts if more of the surface could be made active.

In addition to LDH $Ni_{1-x}Fe_xOOH$, there is extensive experimental evidence that amorphous materials can have exception- ally high electrocatalytic activity for the OER.[62,71–81] In fact, a recent report from Vojvodic, Sargent and co-workers showed that amorphous, homogeneously-dispersed multimetal oxygen- evolving electrocatalysts exhibited some of the best OER performance yet to be reported.[81] However, it is not well understood why these amorphous and homogeneously-dispersed materials exhibit such high catalytic activity, nor is it well understood if amorphous structures also exhibit both "fast" and "slow" catalytic sites.

Herein, we set out to develop a catalytically active, well-dispersed, nanoamorphous (Ni,Fe) oxide for use as an OER electrocatalyst in which we can control the Ni : Fe ratio, and determine if amorphous structures give rise to only "fast" catalytic sites. To accomplish this, we developed a microwave-assisted synthesis route for creating nanoamorphous (Ni,Fe) oxide structures. Microwave synthesis routes[81] have been previously used to form nanostructures of iron oxides,[82–85] but to the best of our knowledge microwave synthesis routes of nickel–iron OER catalysts have not been previously reported. We compared the electrochemical activity of this microwave-assisted, nanoamorphous (Ni,Fe) oxide material to a $Ni_{1-x}Fe_xOOH$ that we synthesized via an electrochem-

ical conditioning of crystalline $Fe_{0.2}$:$Ni_{0.8}$ oxide.[55] To measure the kinetics of the active sites directly, we utilized SI-SECM via a masked-electrode technique. Our findings show that on flat electrodes (roughness factor <1.4), the microwave-assisted, nanoamorphous (Ni,Fe) oxide material had a lower overpotential for the OER compared to the crystal-derived oxyhydroxide. Our SI-SECM experiments on the crystal-derived $Ni_{0.8}Fe_{0.2}OOH$ showed the existence of "fast" and "slow" sites (kinetic rate constants of 1.3 s^{-1} and 0.05 s^{-1}, respectively), and the percentage of fast sites (7%) matched well with the iron-metal content. These results are in very good agreement with the study recently performed by Bard and co-workers.[66] However, SI-SECM experiments on the nanoamorphous ($Ni_{0.8}Fe_{0.2}OOH$) structure showed only one type of site, and the kinetic rate constant of this site (1.9 s^{-1}) matched well with the kinetics of the "fast" site on the crystal-derived Ni0.8- Fe0.2OOH. This finding suggests that well-dispersed, amorphous materials may have higher catalytic activity because they exhibit only the "fast" catalytic sites.

2.2 Materials and Methods

2.2.1 Chemicals

Iron(III) nitrate nonahydrate (98%+, ACS Reagent, Acros), nick- el(II) nitrate hexahydrate (99%, Fisher Scientific), iridium(III) chloride (99.99%, Alfa Aesar), sodium hydroxide (¿97%, Fisher Scientific), ethylene glycol (99.8%, anhydrous, Sigma Aldrich),sodium bicarbonate (Fisher Scientific), potassium hydroxide (85%, Acros Organics), iron(III) sulfate hydrate (Reagent Grade, Alfa Aesar), triethanolamine (97%, Acros Organics) were all used as received without additional purification.

2.2.2 Catalyst Synthesis

Crystalline-derived Catalyst

Crystalline thin-films of $Fe_{0.2}$:$Ni_{0.8}$ oxide were made similar to those previously reported.[85] Briefly, two solutions, one of 0.02 M $Ni(NO_3)_2 \cdot 6\,H_2O$ and the other of 0.02 M $Fe(NO_3)_3 \cdot 9\,H_2O$, were prepared separately in ethylene glycol and subsequently mixed in an 8 : 2 ratio. The solution was dropcast and annealed on Fluorine- doped tin oxide (FTO) coated glass (Sigma-Aldrich) to

create the $Fe_{0.2}$:$Ni_{0.8}$ oxide as described in Supporting Information section. The oxide was then electrochemically conditioned by applying an oxidation current of ca. 10 mA cm^{-2} for 1 hour, as has been previously described.[55]

Nanoamorphous Microwaved-assisted Catalyst

First, a nanoamorphous Fe catalyst was synthesized using a sol–gel method similar to a previously reported method with some modifiations.[86,87] Briefly, 8.08 grams of $Fe(NO_3)_3 \cdot 9\,H_2O$ was dissolved in 100 mL of 18.2 M Ω water. Separately, 1.99 grams of $NaHCO_3$ was dissolved in 100 mL of 18.2 M Ω water. Both solutions were sonicated until fully dissolved. The $Fe(NO_3)_3 \cdot 9\,H_2O$ was placed in a 250 mL Erlenmeyer flask with a Teflon stir bar and placed on a stir plate. The $NaHCO_3$ was placed in a burette and was used to titrate at a rate of 2–3 drops per second to achieve a rate of 2.5–3 mL min^{-1} while rapidly stirring the $Fe(NO_3)_3$ solution. The suspension underwent a gradual color change from orange to deep red at the end. The total titration time was about 40–45 minutes, and the solution continued to stir for one hour after titration. This suspension was then placed in Nalgene bottles to be microwaved. The solution was microwaved for about two minutes, with swirling every 15–20 seconds to mix the contents, in a conventional 1050 W microwave (Rival). After two minutes of microwaving, the solution had begun to boil with bubbles on the sides of the bottles. To form the nanoamorphous Ni catalyst, this procedure was repeated by replacing the $Fe(NO_3)_3 \cdot 9\,H_2O$ with 5.82 grams of $Ni(NO_3)_2 \cdot 6\,H_2O$. After microwaving the nickel suspension, some separation occurred. To form the nanoamorphous mixed- metal catalysts, this procedure was repeated except the $Ni(NO_3)_2 \cdot 6\,H_2O$ and $Fe(NO_3)_3 \cdot 9\,H_2O$ were mixed to create two additional solutions at $1:1$ and $8:2$ molar ratios, respectively. These solutions were titrated and microwaved as described above. Some separation also occurred in the nanoamorphous mixed-metal suspensions. Electrodes were made by dropcasting the suspensions, both with and without the microwave step, on FTO-coated glass and were dried at 70°C as described in the Supporting Information section. After dropcasting, the samples were gently rinsed with 18.2 M Ω water to remove any material that was not well adhered to the surface. This left a nearly transparent film of the nanoamorphous $Ni_{1-x}Fe_xOOH$ catalyst on the FTO-coated glass. Additionally, the microwave-assisted nanoamorphous $Fe_{0.2}$:$Ni_{0.8}$ was deposited via electrophoretic deposition on FTO-coated glass to compare to the dropcast samples on FTO. The nanoamorphous $Fe_{0.2}$:$Ni_{0.8}$ was also electrophoretically de-

posited onto a glassy carbon rotating disc electrode (RDE) for benchmarking, and solution-derived (non-microwaved) and microwave-assisted $Fe_{0.2}$:$Ni_{0.8}$ were dropcast on a glassy carbon RDE for comparison. Electrophoretic deposition was performed by applying -5 V to the working electrode for 10 minutes in a two electrode system with a Ti counter electrode.

2.2.3 Materials Characterization

Scanning electron microscope (SEM) images and Energy Dispersive X-ray Spectrometry (EDS) images were obtained using a FEI Versa 3D Dual Beam SEM. X-ray Diffraction (XRD) data were collected on a Bruker D8 Discover with DaVinci diffractometer, in the standard Bragg–Brentano para-focusing configuration utilizing sealed tube CuKα radiation (λ=1.5418 Å) operated at 40 kV and 40 mA. The sample was mounted using a zero background holder (ZBH) on a horizontal sample stage for an 830 mm diameter goniometer equipped with a 1D Lynxeye detector. Data were collected using a step width of 0.02° and step time of 0.3 s with a 2θ range of 20.0° - 100.0°. X-ray photoelectron spectroscopy (XPS, Physical Electronics, Inc USA) was used to obtain binding energies of the C 1s, O 1s, Fe 2p, and Ni 2p orbitals using a monochromatic Al X-ray source. The adventitious carbon 1s binding energies for all XPS measurements were taken to be 284.8 eV.

2.2.4 Electrochemical Characterization

Cyclic voltammetry (CV) was performed on the catalyst coated FTO electrodes in a custom Teflon cell with a holding place for a Ag/AgCl reference electrode with porous Teflon tip (CH Instruments). The size of all FTO glass working electrodes was 0.49 cm^2, except for those used in the non-microwaved vs microwaved comparison (see Figure 2.1), which were 0.97 cm^2. A 200 μm Pt wire (Electron Microscopy Instruments) was used as the counter electrode, and the CV experiments were performed in 1 M NaOH. All electrochemical measurements were obtained via a CH Instruments (Austin, TX) potentiostat.

Benchmarking experiments (i.e. cyclic voltammetry, chronopotentiometry, chronoamperometry) were performed on a catalyst coated glassy carbon custom rotating disc electrode (RDE), 0.071 cm^2, in a glass cell with a Ag/AgCl reference electrode with porous Teflon tip (CH Instruments) and a Pt counter electrode (CH Instruments). All RDE experiments were operated at 1600rpm in 1M NaOH.

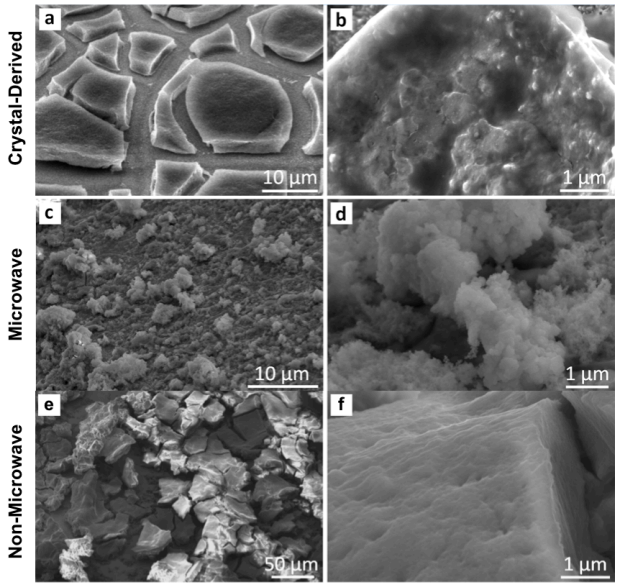

Figure 2.1. Scanning Electron Microscopy (SEM) images of the crystal- derived (a and b), microwave-assisted (c and d), and solution-derived (non-microwaved) (e and f) $Fe_{0.2}$:$Ni_{0.8}$ catalysts deposited on FTO-coated glass.

2.3 Results and Discussion

2.3.1 Materials Synthesis

Figure 2.2 compares the synthesis routes of the nanoamorphous (Ni,Fe) oxide using our newly reported microwave-assisted technique, to the synthesis route of the crystal-derived $Ni_{1-x}Fe_xOOH$. Both techniques start with iron nitrate and nickel nitrate precursors. To fabricate the crystal-derived $Ni_{1-x}Fe_xOOH$, we utilized a previously reported method where Fe-doped NiO rock salt structures are converted to nickel–iron oxyhydroxides via electrochemical conditioning.[66] The rock salt structure (see XRD analysis under Materials characterization) was fabricated by depositing solutions of these nitrate salts in ethylene glycol on a fluorine-doped tin oxide (FTO) coated glass substrate, followed by annealing in air at 525℃ for 3 hours.[81] To fabricate the nanoamorphous structure, we needed to devise a method that allowed us to control the Ni : Fe ratio and form the oxide structure without excessive heating to avoid crystallization and segregation. To accomplish this, we used a titration technique to form nickel–iron carbonates, and then applied a microwave-heating step to decompose the carbonate and form an amorphous oxide structure. For example, when an aqueous solution containing $Fe(NO_3)_3$ is titrated with $NaHCO_3$, the iron and carbonate ions will form iron(III) bicarbonate (2.1), which spontaneously decomposes to iron(III) carbonate

as a precipitate (2.2) (see XPS analysis under Materials characterization). Iron(III) carbonate is inactive for the OER, but it decomposes further to produce the active iron oxide (2.3) at temperatures below 100℃ .[87] We utilized the microwave-heating step to force the decomposition of the carbonate species to the oxide species while still in solution, so that the crystallization and segregation do not occur.

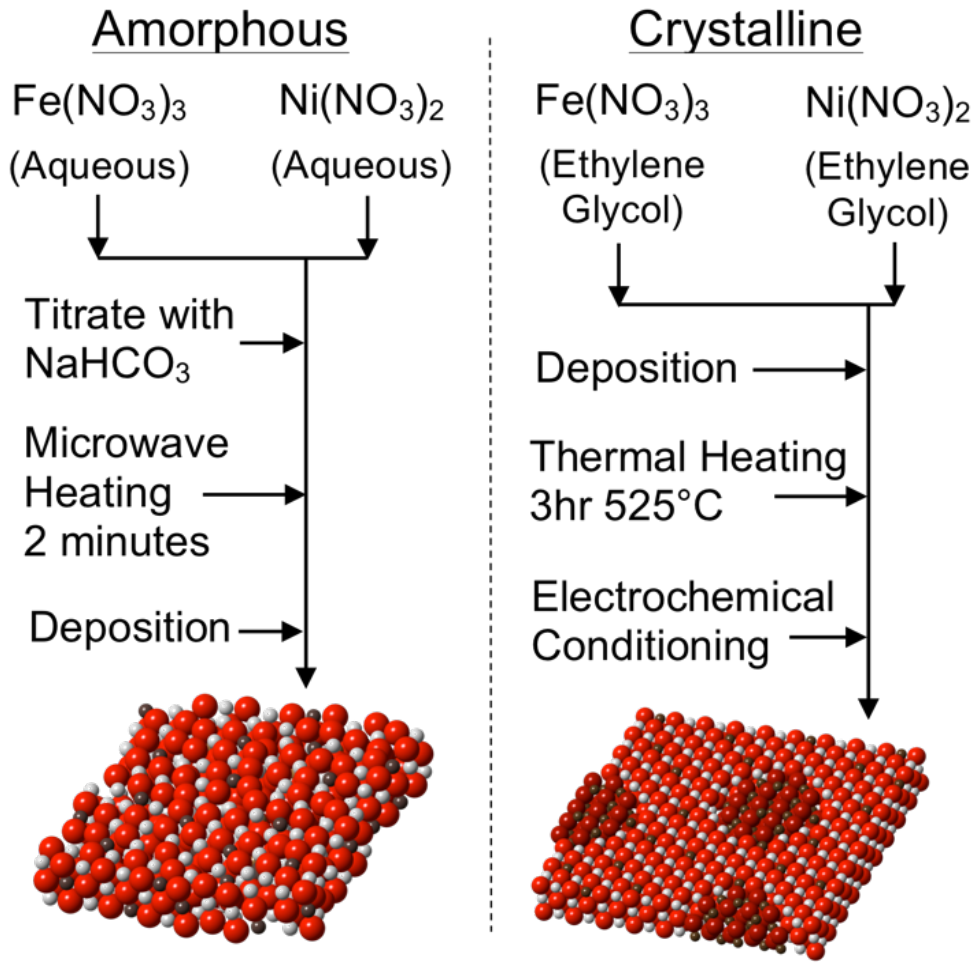

Figure 2.2. Synthesis sequence of nanoamorphous $Fe_{0.2}$:$Ni_{0.8}$ oxide (left) and crystal-derived $Fe_{0.2}$:$Ni_{0.8}$ oxyhydroxide (right).

$$Fe_3{}^+ + 3HCO^- \longrightarrow Fe(HCO_3)_3 \tag{2.1}$$

$$2Fe(HCO_3)_3 \longrightarrow Fe_2(CO_3)_3 + 3CO_2 + 3H_2O \tag{2.2}$$

$$Fe_2(CO_3)_3 \longrightarrow ironoxides + 3CO_2 \tag{2.3}$$

2.3.2 Materials Characterization

SEM images of the crystal-derived $Fe_{0.2}$:$Ni_{0.8}$ prior to electrochemical conditioning (Figure 2.1a) show a catalyst layer with some catalyst cracking occurring due to the annealing step. This formed macroparticles ca. 10's of mm in size. These macroparticles have some porosity and are not single crystals (Figure 2.1b). EDS measurements show a uniform distribution of Fe and Ni in these macroparticles (Supporting Information Figure 2.14), and show that the nickel to iron ratio is approximately $Fe_{0.2}$:$Ni_{0.8}$. SEM images of the solution-derived (non-microwaved) structure (Figure 2.1e and Figure 2.1f) show uniform macroparticles of ca. 50–100 mm in size. These macroparticles are fairly smooth with little surface variation. When the microwave-heating step was applied, the structure changes into an amorphous network, presumably from the release of CO2 that occurs during the decomposition of the carbonate species (Figure 2.1c and Figure 2.1d). EDS measurements on the microwave-assisted structure also show uniform distribution of Fe and Ni and an approximate nickel to iron ratio of $Fe_{0.2}$:$Ni_{0.8}$ (Supporting Information Figure 2.15).

High resolution transmission electron microscopy (HRTEM) images (Figure 2.3) show that the microwave-assisted $Fe_{0.2}$:$Ni_{0.8}$ is not a collection of individual particles but it is a nanoamorphous network. Complete absence of crystalline order is seen even at the 5 nanometer scale (Figure 2.3d). Electron diffractograms (Figure 2.3, inlays) show no diffraction spots, indicating that our microwave- assisted $Fe_{0.2}$:$Ni_{0.8}$ is indeed nanoamorphous. XRD (Figure 2.4a) on the crystal-derived $Fe_{0.2}$:$Ni_{0.8}$ oxide prior to electrochemical conditioning shows the NiO rock-salt structure in addition to Fe_3O_4. Segregation of iron and nickel has been previously reported on nickel–iron samples that have molar ratios very near to the 25% iron segregation limit.[65,66] XRD on the microwave- assisted structure shows an amorphous structure with no iron oxide, nickel oxide, or oxyhydroxide peaks visible, confirming that this material is amorphous. The only diffraction peaks observed are those of $NaNO_3$, which is a remnant of the titration of $Fe(NO_3)_3$ or $Ni(NO_3)_2$ with $NaHCO_3$. The $NaNO_3$ crystals can be seen on SEM images of un-rinsed samples (Supporting Information Figure 2.16).

XPS was performed on the crystal-derived $Fe_{0.2}$:$Ni_{0.8}$ oxide prior to conditioning (Figure 2.4b–e, top spectrum), electrochemically conditioned crystal-derived $Fe_{0.2}$:$Ni_{0.8}$ oxyhydroxide (Figure 2.4b–e,

second spectrum), solution-derived (non-microwaved) $Fe_{0.2}$:$Ni_{0.8}$ (Figure 2.4b–e, third spectrum), and microwave-assisted nanoamorphous $Fe_{0.2}$:$Ni_{0.8}$ (Figure 2.4b–e, bottom spectrum). On the crystal-derived sample prior to conditioning, the Fe 2p3/2 binding energy was 711 eV, which is consistent with the binding energy for Fe_3O_4.[88] Three separate O 1s peaks are visible at binding energies of 528.8 eV, 530.0 eV, and 531.6 eV. The 528.8 eV peak is consistent with iron oxides and/or hydroxide species, and the 530 eV and 531.6 eV peaks are consistent with nickel oxide and/or hydroxide species.[60,89] The Ni 2p3/2 binding energies were 854.5 eV and 856.5 eV. The 854.5 eV peak is consistent with NiO, and the 856.5 eV peak is consistent with NiO or nickel hydroxide.[60,89] The multiple oxygen and nickel peaks confirm that some segregation occurs during the synthesis of the crystal-derived structure prior to conditioning as also shown with the XRD data. The electrochemically conditioned crystal-derived sample shows similar characteristic peaks, and the two separate O 1s peaks suggest that segregation still exists in the crystalline nickel–iron oxyhydroxide structure.

On the microwave-assisted structure, the Ni 2p3/2 binding energy was 855.9 eV, indicative of $Ni(OH)_2$ or NiOOH.[60,89] The single O 1s peak at a binding energy of 531.2 eV is indicative of nickel oxide, nickel hydroxide, or iron hydroxide species.[59,60,88,89] The Fe 2p3/2 binding energy of 711.1 eV is also indicative of an iron binding energy in a hydroxide structure.[88] However, the solution-derived (non-microwaved) binding energies contain a crucial difference when compared to that of the microwave-assisted. On the non-microwaved sample, there is a C 1s binding energy at 289.2 eV, which is not present on the microwave-assisted structure. The 289.2 eV peak is consistent with a carbonate peak,58 which gives strong evidence to support the formation of an inactive iron carbonate species in the initial steps of the synthesis preceding the microwave step. In addition, this XPS data is further evidence that the microwave- assisted synthesis is able to create a nickel–iron structure with no measurable segregation of iron.

2.3.3 Electrochemical Characterization

Rotating disc electrode (RDE) cyclic voltammograms of solution- derived (non-microwaved) and microwave-assisted $Fe_{0.2}$:$Ni_{0.8}$ on a glassy carbon electrode, along with bare glassy carbon are shown in Figure 2.5 a. Here the utility of the microwaving step is apparent. The activity of the non-microwaved (i.e. carbonate) material over the bare glassy carbon is marginal. However,

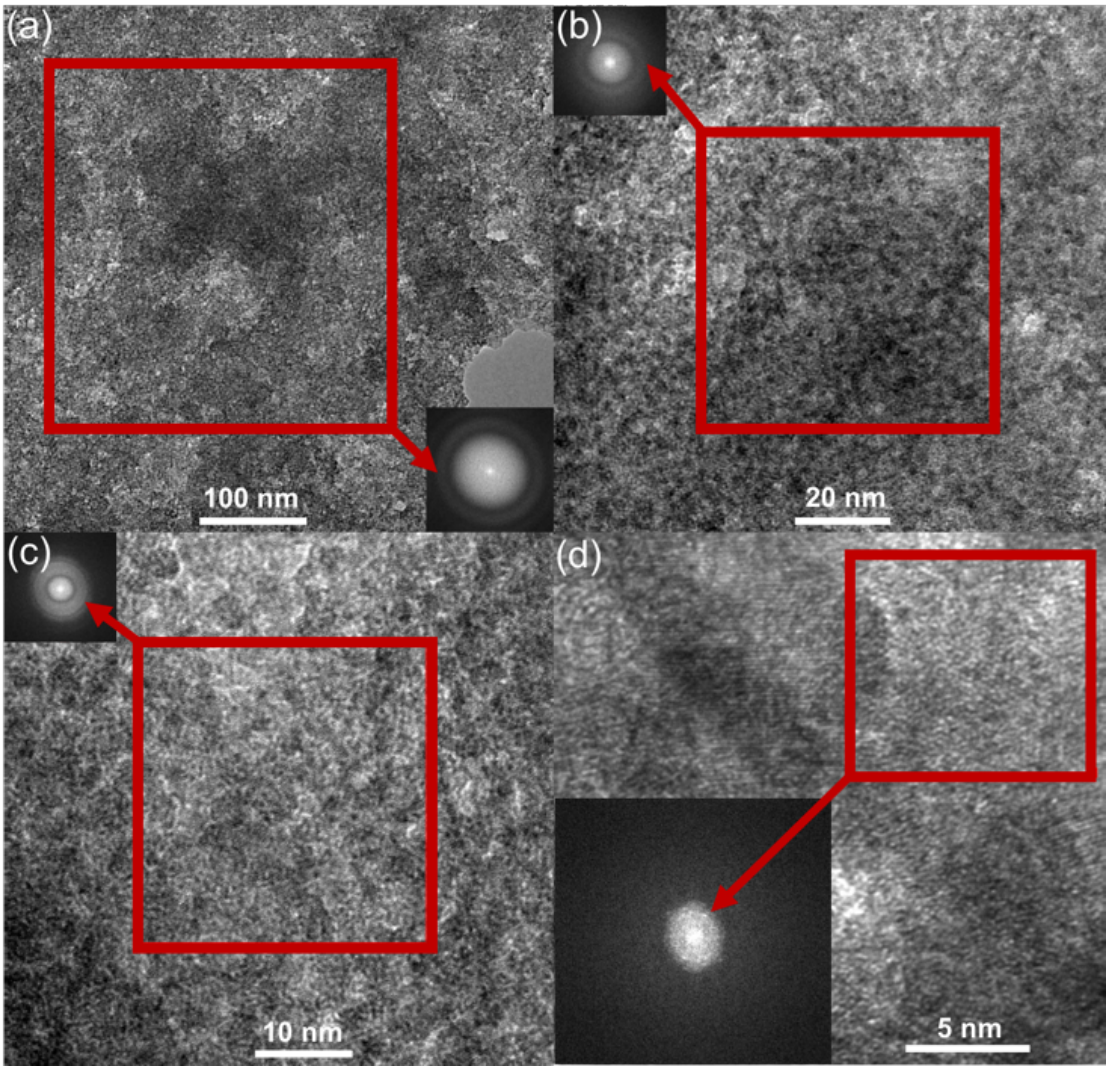

Figure 2.3. High resolution transmission electron microscopy (HRTEM) images of the microwave-assisted nanoamorphous $Fe_{0.2}$:$Ni_{0.8}$ (a–d) with the corresponding electron diffractograms (inlays).

the catalytic activity of the microwave-assisted structure shows a dramatic improvement compared to the non-microwaved structure. We also utilized two deposition techniques to apply the microwave-assisted sample to the GC electrode, electrophoretic deposition and dropcasting (MW-E and MW-D, respectively), and found that electrophoretic deposition (electrodeposition) provided better catalyst coverage and higher catalytic activity, with the MW-E electrode reaching 100 mA cm^{-2} at 369 mV overpotential.

To further demonstrate the utility of the microwave-step, we compared the catalytic activity of the non-microwaved and microwave-assisted structures of mixed-metal $Ni_{1-x}Fe_xOOH$ with different Ni : Fe ratios (representative cyclic voltammograms are shown in Figure 2.5b). We observed that

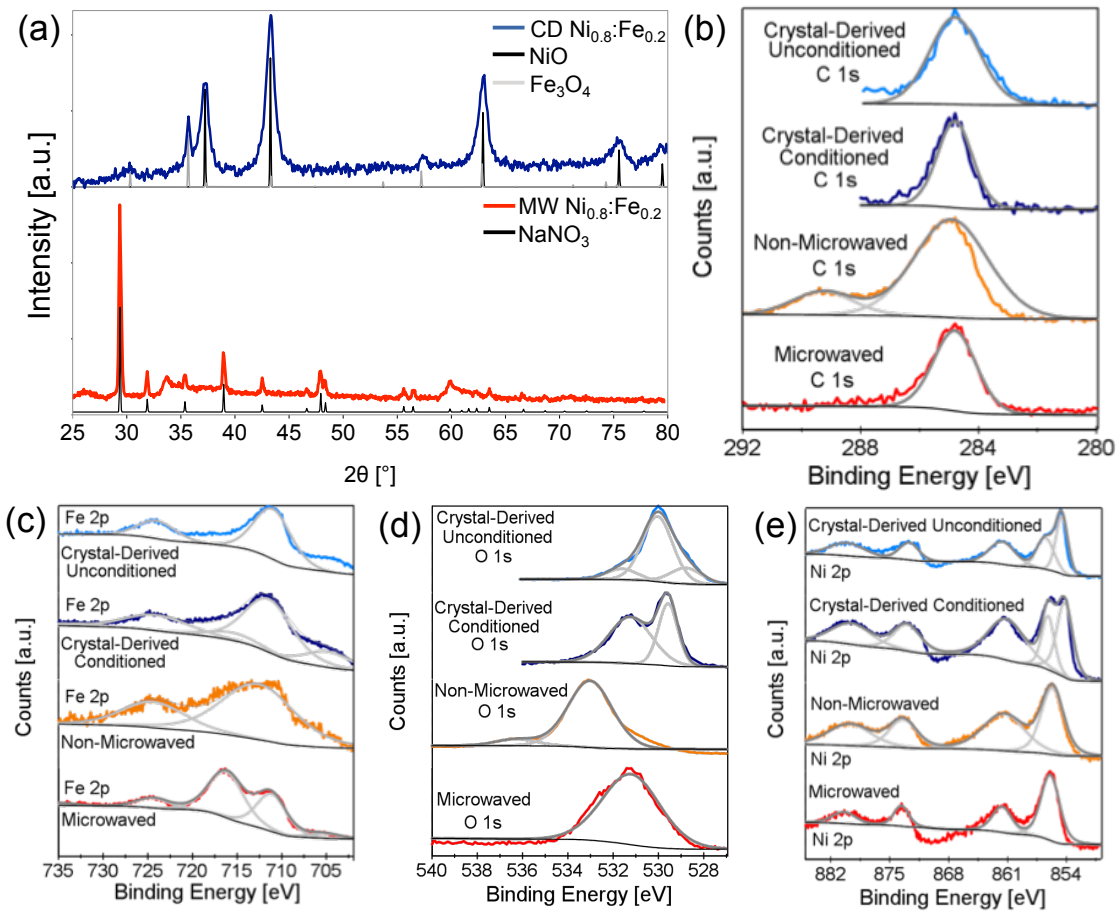

X-ray diffraction of crystal-derived $Fe_{0.2}$:$Ni_{0.8}$ oxide prior to electrochemical conditioning and microwave-assisted nanoamorphous $Fe_{0.2}$:$Ni_{0.8}$ powders (a). X-ray photoelectron spectroscopy of the crystal-derived $Fe_{0.2}$:$Ni_{0.8}$ oxide prior to conditioning (b–e, top spectrum), electrochemically conditioned crystal-derived $Fe_{0.2}$:$Ni_{0.8}$ oxyhydroxide (b–e, second spectrum), solution-derived (non-microwaved) $Fe_{0.2}$:$Ni_{0.8}$ (b–e, third spectrum), and microwave-assisted nanoamorphous $Fe_{0.2}$:$Ni_{0.8}$ (b–e, bottom spectrum).

Figure 2.4.]

the non-microwaved samples containing Fe (Fe, Ni:Fe, and $Fe_{0.2}$:$Ni_{0.8}$) did not have any significant catalytic activity for the OER, nor did we observe the $Ni(OH)_2$/NiOOH redox peaks typically found in Ni:Fe oxy- hydroxides[51,52] for these samples (Supporting Information Figure 2.8 and Figure 2.9). For all of the $Ni_{1-x}Fe_xOOH$ microwave-assisted structures, we observed the Ni(OH)2/NiOOH redox peaks (see Supporting Information Figure 2.10) and a large oxidation current indicative of catalytic activity for the OER. The solution-derived and microwave-assisted samples that only contained Ni also exhibited both of these characteristics. Since we made no attempt to purify the Ni precursors, we attribute the relatively high activity of the Ni-only samples to Fe impurities that may be

present. Triplicate cyclic voltammetry measurements from different synthesis batches show good reproducibility for all microwave-assisted structures (Supporting Information Figure 2.11).

To compare the MW-E and MW-D $Fe_{0.2}$:$Ni_{0.8}$ to the crystal- derived $Fe_{0.2}$:$Ni_{0.8}$ oxyhydroxide and crystalline IrOx, cyclic voltammograms were performed with all samples deposited onto FTO-coated glass (Figure 2.5c). Both the microwave-assisted and crystal-derived samples show the Ni(OH)2/NiOOH redox peaks and the large oxidation current indicative of catalytic activity for the OER. The IrOx sample also shows a small wave, which may be attributed to a IrIV/IrV transition,[67] prior to the onset of the large oxidation wave indicative of catalytic activity for the OER. The static cyclic voltammetry measurements show that the MW- E $Fe_{0.2}$:$Ni_{0.8}$ electrode has an overpotential ca. 100 mV less than that of the crystal-derived $Fe_{0.2}$:$Ni_{0.8}$ and ca. 200 mV less than that of crystalline IrOx.

In order to determine if the increase in catalytic activity of the microwave-assisted electrodeposited $Fe_{0.2}$:$Ni_{0.8}$ samples was due to an increase in the electrochemical surface area (ECSA), the double layer capacitance was measured via cyclic voltammetry (Supporting Information Figure 2.12 and Figure 2.13). We measured similar and very low roughness factors on both the crystalline $Ni_{0.8}Fe_{0.2}OOH$ and the microwave-assisted nanoamorphous $Fe_{0.2}$:$Ni_{0.8}$ structures, 1.2 and 1.4, respectively. Reliable estimation of the ECSA of a catalyst can be difficult and subjective, but based on these measurements, it cannot be conclusively stated that a change in the ECSA is the reason for the increase in electrocatalytic performance of the microwave-assisted structure. In addition, we measured a slightly higher mass loading with the crystal- derived sample having 120 $\pm$ 20 μg cm^{-2} and the microwave- assisted sample having 60 $\pm$ 20 μg cm^{-2}. This suggests that the increased electrocatalytic activity of the microwave-assisted structure is not simply due to an increase in the ECSA or an increase in the mass loading.

While, the microwave-assisted $Fe_{0.2}$:$Ni_{0.8}$ sample showed an OER overpotential of 250 mV at 10 mA cm^{-2}, overpotentials obtained from Figure 2.5c are not at steady-state. This makes comparison difficult due to transient concentration gradients that occur in static cyclic voltammetry experiments. Thus, the overpotential was obtained under steady-state conditions to benchmark the electrocatalytic activity for the OER as articulated by Jaramillo (Figure 2.6).5 The steady-state currents from 30 s chronoamperometry experiments (Figure 2.6, squares) and the steady-state overpotentials from 30 s chronopotentiometry experiments (Figure 2.6, circles) agree well with the

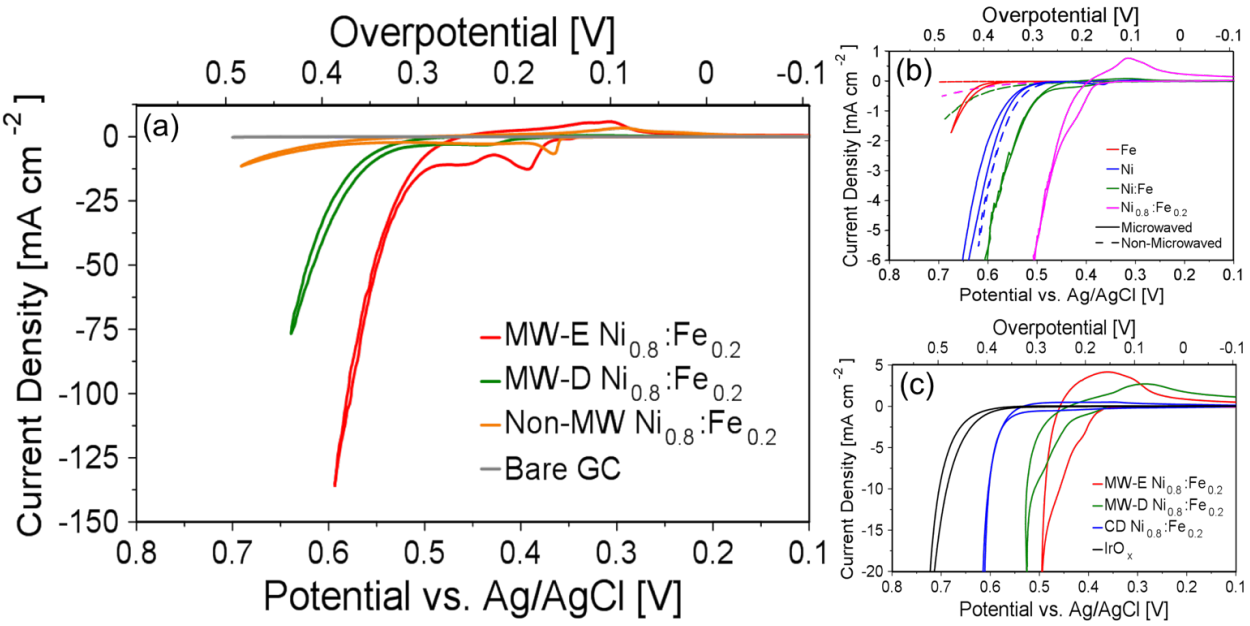

Figure 2.5. Rotating disc electrode cyclic voltammograms of microwave-assisted electrodeposited (MW-E) and dropcast (MW-D) nanoamorphous $Fe_{0.2}$:$Ni_{0.8}$, with solution-derived (Non-MW) $Fe_{0.2}$:$Ni_{0.8}$ on a glassy carbon (GC) electrode at 10 mV s^{-1} (a). Static cyclic voltammograms of solution-derived (non-microwaved) and microwave-assisted Ni_{1-x}:Fe_x on FTO glass at 1 mV s^{-1} (b). Static cyclic voltammograms of MW-E and MW-D nanoamorphous $Fe_{0.2}$:$Ni_{0.8}$ along with crystal-derived (CD) $Fe_{0.2}$:$Ni_{0.8}$ oxyhydroxide and crystalline IrO_x on FTO glass at 50 mV s^{-1} (c). All experiments were performed in 1 M NaOH and are corrected for uncompensated resistance (R_u).

RDE cyclic voltammetry curve (Figure 2.6, solid line). The microwave-assisted nanoamorphous electrodeposited $Fe_{0.2}$:$Ni_{0.8}$ sample had a low overpotential for the OER at 286 mV for 10 mA cm-2 (geometric area), where the overpotential at t = 0 was taken from the chronopotentiometry curve at 30 s. This value is among the lowest overpotentials reported on "flat" electrodes (Supporting Information Table Figure 2.7). A 2 hour chronopotentiometry experiment at 10 mA cm-2 was also conducted to assess the stability of the catalyst. After two hours of applying an overpotential sufficient to produce a current density of 10 mA cm^{-2}, the required overpotential increased only slightly to 315 mV (Figure 2.6, inlay).

2.4 Conclusions

Here we report a microwave-assisted synthesis method to create mixed-metal nanoamorphous nickel–iron catalysts for the OER. We observed that on flat electrodes (roughness factor ¡1.4), the OER electrocatalytic activity was higher on the microwave- assisted, nanoamorphous $Fe_{0.2}$:$Ni_{0.8}$ structure compared to the crystal-derived $Fe_{0.2}$:$Ni_{0.8}$ oxyhydroxide. By benchmarking the microwave-

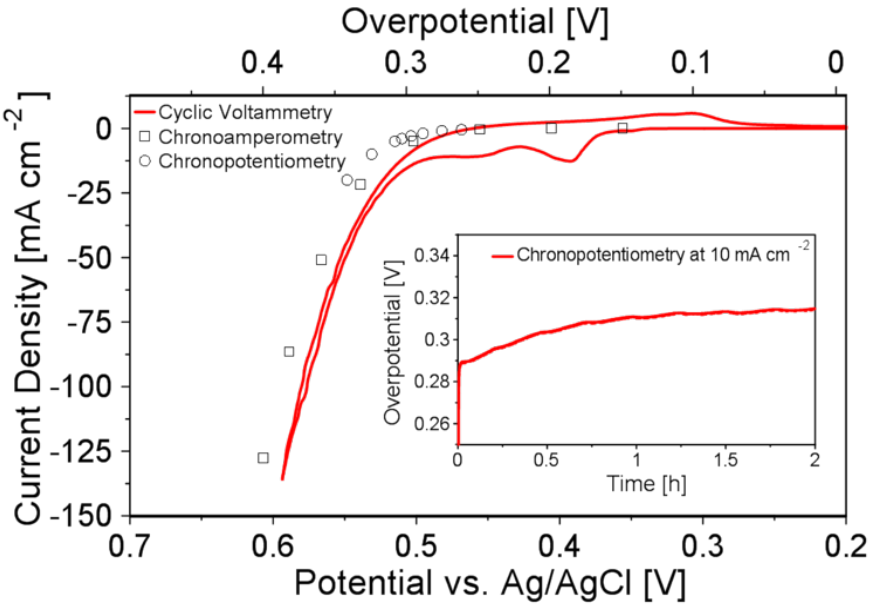

Figure 2.6. Cyclic voltammogram at 10 mV s^{-1} (solid line), steady-state currents from 30 s chronoamperometry experiments (squares), and steady-state potentials from 30 s chronopotentiometry experiments (circles) on microwave-assisted nanoamorphous $Fe_{0.2}$:$Ni_{0.8}$ electrodeposited on a glassy carbon rotating disc electrode (RDE). 2 h chronopotentiometry experiment at 10 mA cm^2 with the microwave- assisted nanoamorphous $Fe_{0.2}$:$Ni_{0.8}$ electrodeposited on a glassy carbon RDE (inlay). All RDE experiments were operated at 1600 rpm in 1 M NaOH and corrected for R_u.

assisted, nanoamorphous structure, we determined that it had a very low overpotential of 286 mV at 10 mA cm^{-2}. We measured the kinetics of the active sites of both the crystal-derived and microwave-assisted $Fe_{0.2}$:$Ni_{0.8}$ samples directly using the surface interrogation mode of scanning electrochemical microscopy (SI-SECM). We determined that the microwave-assisted structure contained all "fast" sites with rate constant 1.9 s^{-1}, and the crystal-derived structure contained 7% "fast" sites with rate constant 1.3 s^{-1} and 93% slow sites with a rate constant of 0.05 s^{-1}. This finding is experimental evidence that developing synthesis methods to maximize the uniformity of amorphous structures is advantageous for the development of highly efficient Ni–Fe catalysts for electrochemical water oxidation.

2.5 Acknowledgement of Contributions

Supplement data obtained by Kelly Song and Dr. Barforoush.

2.6 Supporting Information

2.6.1 Electrode Fabrication

Drop-cast Thin Films

FTO glass sheets (Sigma Aldrich) cut to 0.5-inch squares were cleaned by washing with soap, deionized water, and ethanol. The FTO pieces were placed in a beaker with ethanol and sonicated for 10 minutes. The slides were dried at room temperature for about 5 minutes. Then, using a micropipette, approximately 250 μL of solution was dropped onto each square in the most even thin layer possible. The slides were then placed into an oven at 135 °C for about 30 minutes. This was repeated once more for a second coating. After coating the FTO glass, the crystalline thin-film samples were fired in air at 500 °C for 3 hours with a 1 °C min^{-1} ramp rate. For each sample, a 2-3 mm edge of coating was scraped off and copper wire tape (Electron Microscopy Sciences) was placed on and scored.

Drop-cast solution-derived and microwave-assisted films:

FTO glass sheets were cut and cleaned as described above. Using a micropipette, approximately 250 μL of the suspension was dropped onto each square in the most even thin layer possible. The slides were then placed into an oven at 70 °C for about 30 minutes. This was repeated once more for a second coating. No additional annealing was applied to the electrode. For suspensions where separation occurred, the suspension was pipetted from the bottom of the container.

2.6.2 Synthesis

2.6.3 Crystalline IrO_x:

The crystalline thin-films of IrO_x were made similar to the crystalline-derived $Fe_{0.2}$:$Ni_{0.8}$ described in the main paper. Briefly, a solution of 0.02 M $IrCl_3$ was prepared in ethylene glycol, and the solution was drop-cast and annealed on FTO coated glass (further details can be found in Electrode Fabrication section).

	$\eta_{t=0}$ [mV] (10 mA cm^{-2})	$\eta_{t=2h}$ [mV] (10 mA cm^{-2})	η_{CV}[mV] (10 mA cm^{-2})	η_{CV} [mV] (100 mA cm^{-2})	j_g, [mA cm^{-2}] (η=0.35 V)	j_s, [mA cm-2] (η=0.35 V)	Roughness Factor
This Study	**286**	**315**	**250**	**369**	**61.5**	**55.2**	**1.4**
IrO_x[2]	320 ± 40	1050 ± 20	-	-	42 ± 13	0.4 ± 0.2	105
$NiFeO_x$[2]	350 ± 10	380 ± 20	-	-	15 ± 6	3 ± 2	6
LDH $Ni_{0.9}Fe_{0.1}O_x$[3]	-	-	336	-	-	-	-
Electrodeposited NiFe (40% Fe)[4]	280	-	-	-	-	20 (at 0.3 V)	2-6
LDH NiFe on Graphene Oxide[5]	-	-	221	-	-	-	-
Fractal NiFe[6]	-	-	-	300	-	-	-
Amorphous Ni-Fe oxyhydroxide[7]	300	-	-	-	-	-	-
Pulse-Electrodeposited Ni–Fe (Oxy)hydroxide[8]	-	-	250	-	-	-	-
Laser Ablation $Ni_{0.22}Fe_{0.78}$ LDH[9]	280	-	-	-	-	-	-

Figure 2.7. Performance comparisons between the results of this study and other recent studies on (Ni,Fe) electrocatalysts for the oxygen evolution reaction.

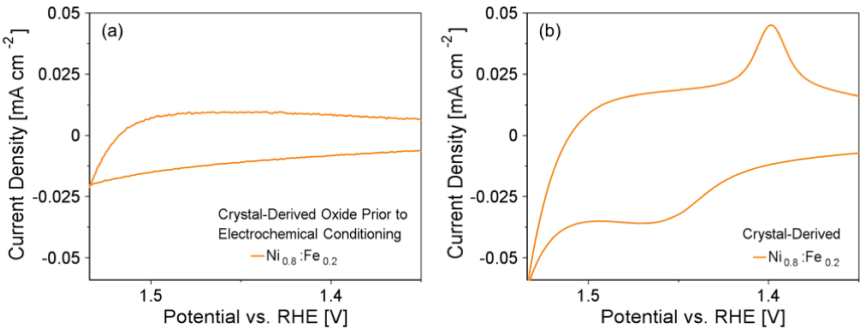

Figure 2.8. Cyclic voltammograms (CVs) of the crystal-derived $Fe_{0.2}$:$Ni_{0.8}$ before (a) and after (b) applying an electrochemical conditioning oxidation current of ca. 10 mA for 1 h to create an oxyhydroxide morphology with characteristic peaks appearing in the CVs between 1.45 and 1.5 V vs RHE. The CV after electrochemical conditioning is a magnified view of the crystal-derived CV presented in Figure Figure 2.4a of the main text.

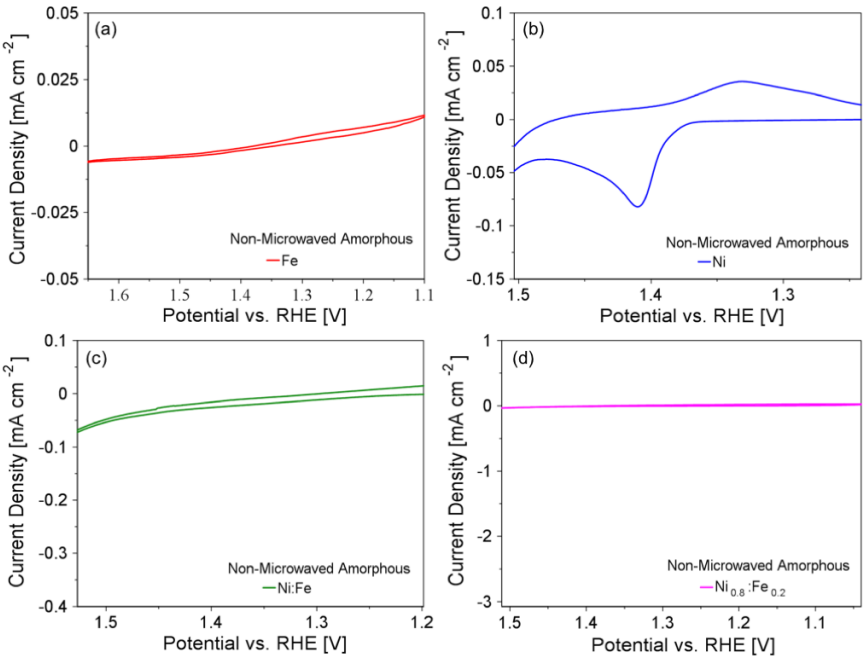

Figure 2.9. Cyclic voltammograms (CVs) of the solution-derived Fe (a), Ni (b), Ni:Fe (c), and $Fe_{0.2}$:$Ni_{0.8}$ (d) on FTO-coated glass. Each CV was taken from Figure Figure 2.1a of the main text and magnified to the region where the Ni^{II}/Ni^{III} peaks would be visible. The Ni is the only one of our solution-derived materials to show the characteristic oxyhydroxide peaks before microwaving.

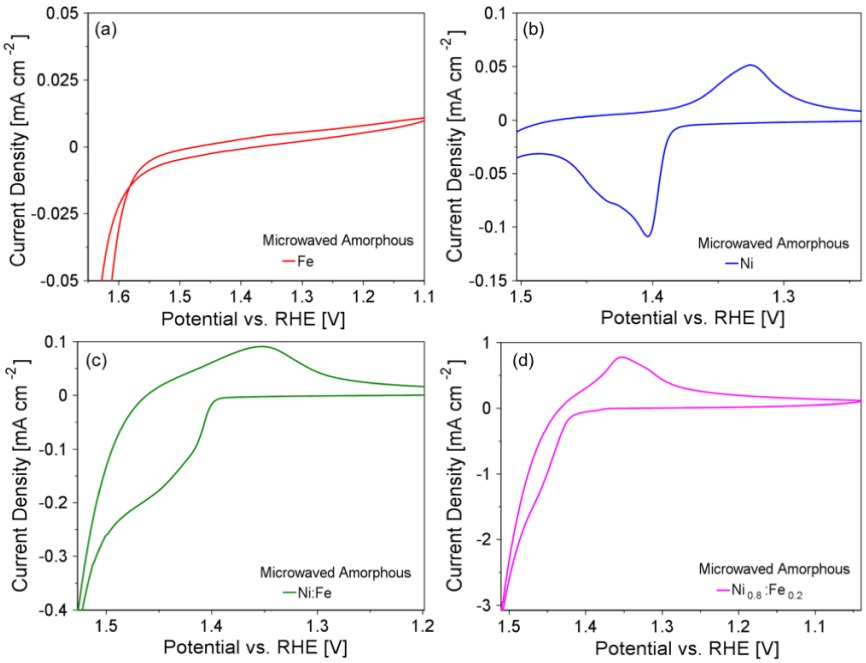

Figure 2.10. Cyclic voltammograms (CVs) of the microwave-assisted Fe (a), Ni (b), Ni:Fe (c), and $Fe_{0.2}$:$Ni_{0.8}$ (d). Each CV was taken from Figure Figure 2.1a of the main text and magnified to the region where the Ni^{II}/Ni^{III} peaks are visible. As expected, the Fe is the only one of our microwave-assisted materials to lack the characteristic peaks.

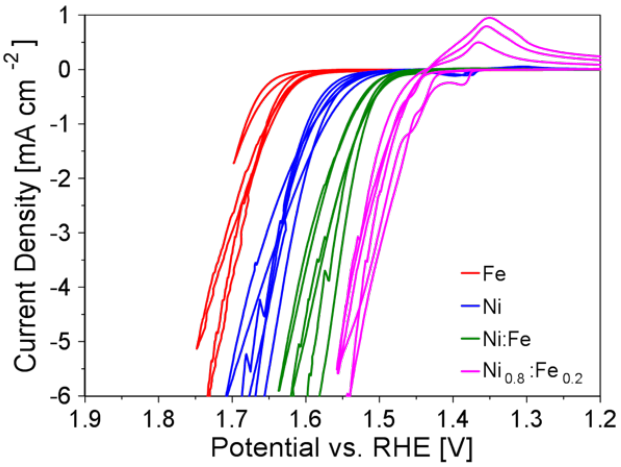

Figure 2.11. Experimental cyclic voltammograms (CVs) in 1 M NaOH at a scan rate of 1 mV s^{-1} not corrected for R_u for three different batches of microwave-assisted Fe, Ni, Ni:Fe, and $Fe_{0.2}$:$Ni_{0.8}$ coated on FTO glass using the convention of reduction currents as positive and negative potentials to the right. Each CV shown is from a freshly fabricated microwave-assisted metal/mixed metal (oxy)hydroxide.

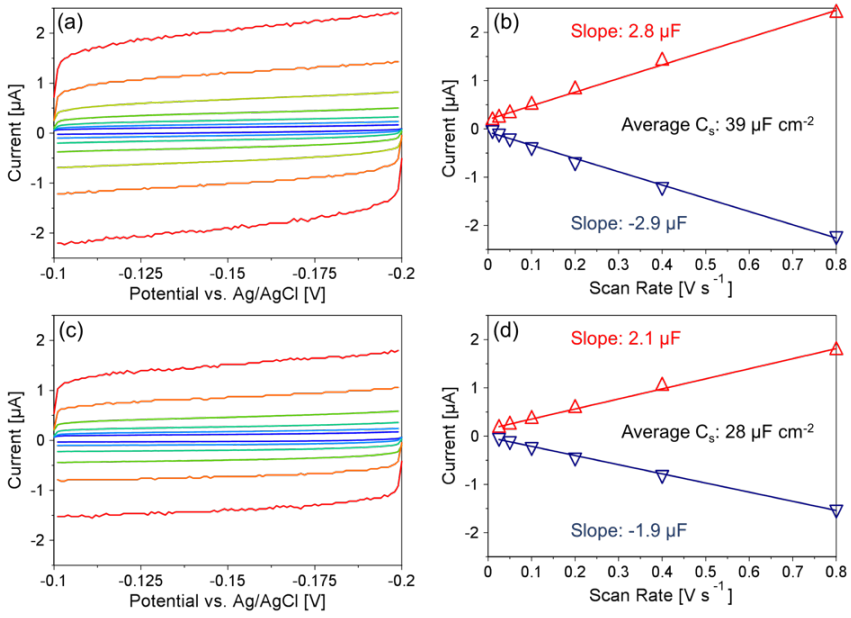

Figure 2.12. Double-layer capacitance measurements via cyclic voltammetry on microwave-assisted $Fe_{0.2}$:$Ni_{0.8}$ electrodeposited on glassy carbon (a) and bare glassy carbon (c) in 1 M NaOH at various scan rates where non-faradaic current occurs. Current vs scan rate for microwave-assisted $Fe_{0.2}$:$Ni_{0.8}$ electrodeposited on glassy carbon (b) and bare glassy carbon (d) with regression lines next to the corresponding double layer capacitance values and the average specific capacitance, C_s.

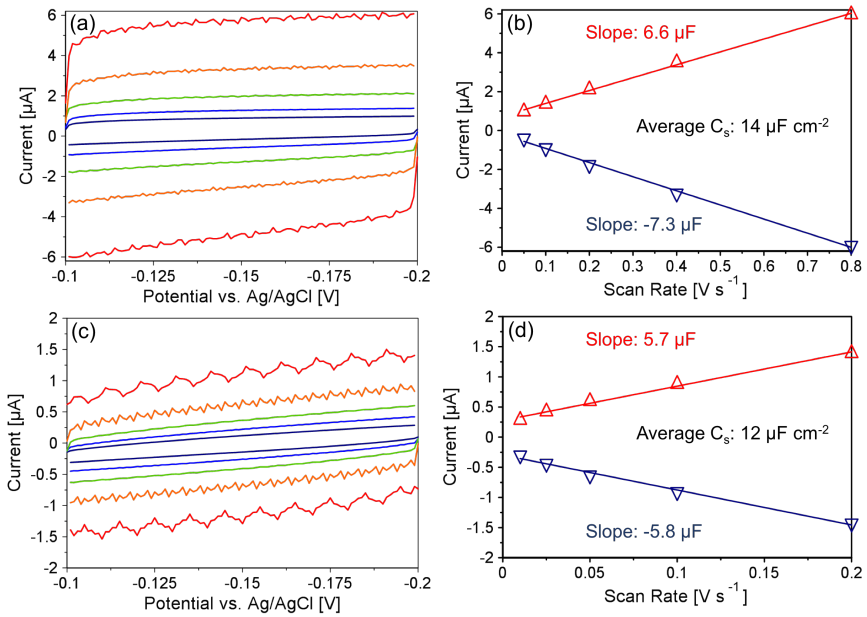

Figure 2.13. Double-layer capacitance measurements via cyclic voltammetry on crystal-derived $Fe_{0.2}$:$Ni_{0.8}$ oxyhydroxide on FTO-coated glass (a) and bare FTO-coated glass (c) in 1 M NaOH at various scan rates where non-faradaic current occurs. Current vs scan rate for crystal-derived $Fe_{0.2}$:$Ni_{0.8}$ oxyhydroxide on FTO-coated glass (b) and bare FTO-coated glass (d) with regression lines next to the corresponding double layer capacitance values and the average specific capacitance, C_s.

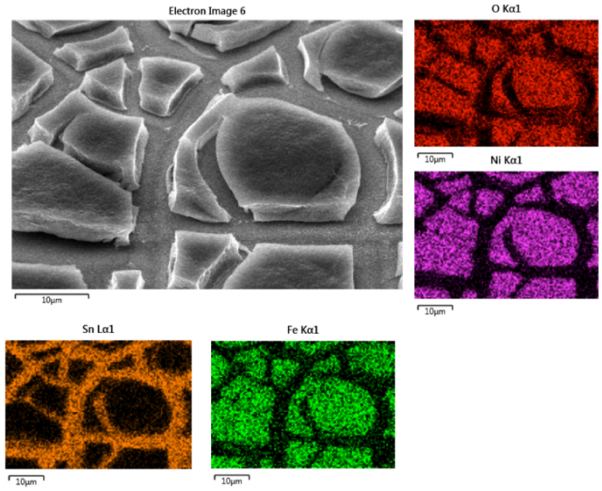

Figure 2.14. SEM and corresponding EDS images of crystal-derived $Fe_{0.2}$:$Ni_{0.8}$ sample prior to electrochemical conditioning step. Shown is the uniform distribution of Fe and Ni along with the Sn of the sub-layer due to the FTO coated glass substrate.

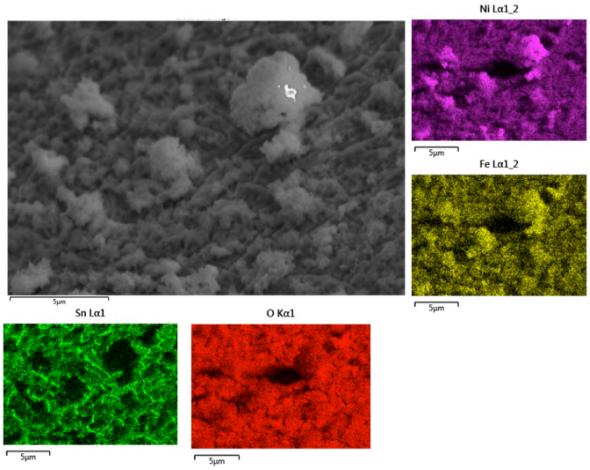

Figure 2.15. SEM and corresponding EDS images of microwave-assisted, nanoamorphous $Fe_{0.2}$:$Ni_{0.8}$ sample electrophoretically deposited on a FTO coated glass substrate. Shown is the uniform distribution of Fe and Ni along with the Sn of the sub-layer due to the FTO coated glass substrate.

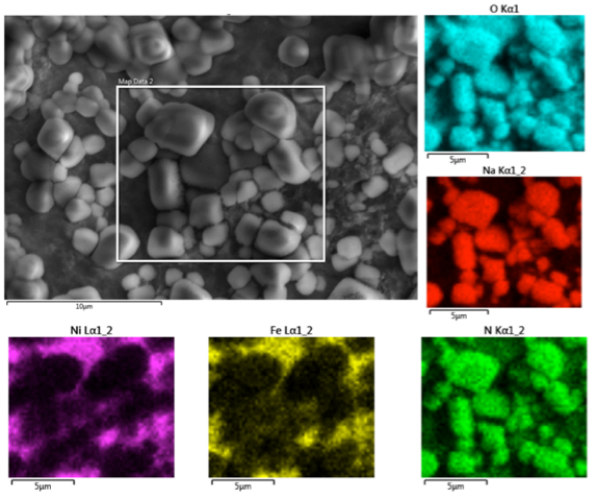

Figure 2.16. SEM and corresponding EDS images of the microwave-assisted $Fe_{0.2}$:$Ni_{0.8}$ sample without the rinsing step. Shown are the $NaNO_3$ crystal that are a result of titration of $NaHCO_3$ with Fe or Ni NO3. These $NaNO_3$ crystals are also present in the XRD patterns of the microwave-assisted samples.

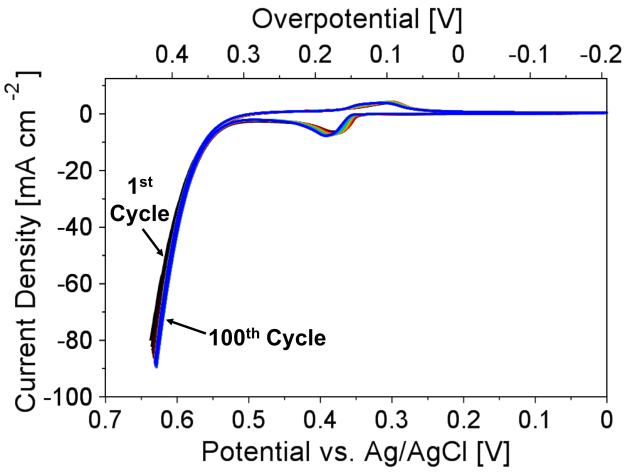

Figure 2.17. 100 cyclic voltammetry (CV) cycles at 50 mV s^{-1} on microwave-assisted nanoamorphous $Fe_{0.2}$:$Ni_{0.8}$ electrodeposited on a glassy carbon electrode in 1 M NaOH and corrected for R_u showing no significant change in activity with each successive cycle.

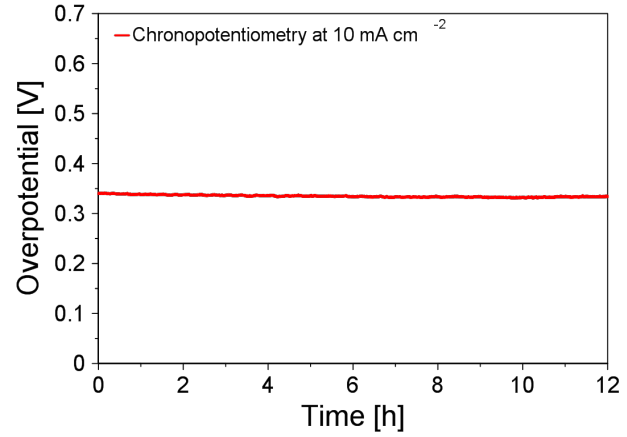

Figure 2.18. 12 h chronopotentiometry experiment at 10 mA cm^{-2} with microwave-assisted nanoamorphous $Fe_{0.2}$:$Ni_{0.8}$ electrodeposited on a glassy carbon RDE at 1600 rpm in 1 M NaOH and corrected for R_u showing stable oxygen production with an overpotential of 0.33 V at 12 h.

2.7 Appendix

The synthesis for the microwave-assisted nanoamorphous $Fe_{0.2}$:$Ni_{0.8}$ oxide yields a suspension in which separation occurs, resulting in a sediment layer (containing the catalyst) beneath an aqueous layer (Figure Figure 3.7). Different combinations of these two layers were used for dropcasting on fluorine doped tin oxide (FTO) glass to determine the most efficient way of depositing the catalyst from solution. Using a pipette, bottom layer:top layer ratios of 60:40, 70:30, 90:10, and 100:0 were dropcast onto FTO glass, and the samples were tested using cyclic voltammetry (CV). There was no apparent advantage in using one ratio over the other so the bottom layer was used in all of the depositions.

Dip-coating was investigated as an alternative to drop-casting nanoamorphous $Fe_{0.2}$:$Ni_{0.8}$ oxide on FTO glass. Using the CNC mill, clean FTO glass was dipped into catalyst solution and removed at a controlled rate. The catalyst suspension would not adhere well the FTO glass when it was removed from the catalyst solution; whereas, drop-casting on FTO glass allowed the catalyst solution to dry onto the electrode and provide sufficient adhesion for electrochemical characterization.

Different methods of drying the drop-cast nanoamorphous $Fe_{0.2}$:$Ni_{0.8}$ oxide on FTO were also investigated, including drying in the oven at 70 °C and 120 °C, air overnight, and UV lamp. At 120 °C, the coating would be thicker around the edges and absent in the center, possibly due to drying too quickly, and the UV lamp did not produce consistent results. Oven drying at 70 °C gave identical results to air drying overnight, so oven drying at 70 °C was used to dry drop-cast samples.

Voltage and electrodeposition time were varied to find the optimum conditions for electrodeposition. Electrodeposition at -2 volts was insufficient to form a catalyst layer on the FTO glass while -5 V formed a catalyst layer. Based on cyclic voltammograms (CVs), samples electrodeposited at -10 V did not show better performance than those electrodeposited at -5 V. Electrodeposition at -5 V was performed over 5, 10, 15, 20, 30, and 60 minute time periods. Samples prepared from 5 minutes of electrodeposition showed poor performance compared to those prepared from 10 minutes of electrodeposition, indicating insufficient catalyst coverage. Longer electrodeposition times, such as 30 minutes and 60 minutes, also produced samples with poor coverage.

Chapter 3

Nanoamorphous FeNi Electrocatalyst on Porous, High Surface Area Nickel Foam for Oxygen Evolution Reaction

3.1 Introduction

The rising global demand for clean energy combined with the depletion of fossil fuels, the world's major energy resource, has sparked great interest in alternative energy sources that are both renewable as well as environmentally friendly.[90,91] In particular, hydrogen is a highly favored avenue for carbon-neutral fuel if produced via water electrolysis using renewable energy such as solar or wind.[92,93] Electrolyzing water is a quick to start and easy to use process for hydrogen production. It is particularly significant when using renewable energy sources as it maximizes the potential for the excess energy generated during "down" times and produces hydrogen in high purities up to 99.8%.[94] Alkaline water electrolyzers are currently the most common type in practice. They are favored for low cost and high efficiency leading to higher purities.[95]

The foremost challenge in water electrolysis is the efficiency limiting oxygen evolution reaction (OER) half reaction which requires a high potential due to slow kinetics for the complex four-electron/four-proton transfer.[24,96] Prior/initial studies on water electrolysis concluded precious, expensive metal oxides such as IrO_2 and RuO_2 in acidic media were the most active OER electro-

catalysts.[16–19] Recent research has identified transition metal oxides such as Mn, Fe, Co, Ni, Mo, and W to hold promising activity in alkaline media for the OER.[20–22] More specifically, Fe and Ni electrocatalysts have shown significantly increased activity when combined for OER as opposed to the metals individually.[27,97–99]

Yet, studies have reported conflicting results for the optimal ratio of Fe:Ni.[30,61,100,101] Bell and co-workers reported a limit to the percentage of Fe to be ca. 25% where exceeding that would cause segregation.[30] In an earlier study, our group disclosed a facile microwave-assisted synthesis procedure to obtain a nanoamorphous mixed metal oxide structured electrocatalyst specifically for an $Fe_{0.2}$:$Ni_{0.8}$ mixture based on Bell's work.[29,102] Building on this previous work, we discovered the method can be applied to a wide array of metals and ultimately be used as a general technique for producing metal oxide/(oxy)hydroxide electrocatalysts. This will allow for many different combinations of mixed metal electrocatalysts to be synthesized and tested. Additionally, as the electrocatalyst is heated in the microwave during the synthesis, this method allows for deposition on a variety of supports in the electrocatalysts "final" structure/without any further structural modifications/heating.

Recently, Alexis T. Bell identified that a major challenge for improving OER activity with FeNi based electrocatalysts is obtaining a multidimensional/3-D layered electrocatalyst that is markedly porous for a certain anode surface. Meanwhile, a study conducted by Vojodic and Sargent indicates that homogeneously dispersed and amorphous multimetal electrocatalysts yielded some of the best OER performance to date.[103] Based on our broadly applicable synthesis route we set out to combine the work of Vojodic and Sargent with the grand challenge proposed by Bell to further improve the performance of an OER electrocatalyst and thereby increasing the efficiency of the OER in the pursuit of hydrogen fuel production.

In this work, we aspired to further improve our microwave-assisted nanoamorphous mixed metal oxide electrocatalyst $Fe_{0.2}$:$Ni_{0.8}$ performance. First, we tested various combinations of reported transition metals using our developed synthesis method to both confirm our technique as widely applicable as well as searching for an OER activity exceeding/surpassing previously reported overpotential of ca. 280 mV at 10 mA/cm^2. Then using the champion of these trials, we pursued the challenge proposed by Bell to obtain a 3D porous nanoamorphous electrocatalyst deposited on a high surface area support in order to achieve a high performing OER electrocatalyst. Ultimately,

we demonstrate herein a facile strategy that is generalized to any metal to fabricate 3D nanoamorphous electrocatalyst which can be deposited onto a high surface material support to achieve one of the lowest reported overpotentials.

3.2 Experimental

3.2.1 Materials

Iron (III) nitrate nonahydrate (98%+, ACS Reagent, Acros), nickel (II) nitrate hexahydrate (99%, Fisher Scientific), cobalt (II) nitrate hexahydrate (98%+, ACS Reagent, Acros), ammonium metatungstate hydrate (Strem Chemicals), ammonium molybdate (VI) tetrahydrate (ACS Reagent, Acros), sodium hydroxide (Fisher Chemical), and sodium bicarbonate (Tech, Fisher Science Education) were all used as received without any additional purification. Fluorine doped tin oxide (FTO) coated glass slides with ca. 7Ω surface resistivity were obtain from Aldrich Chemistry. Carbon weave paper and nickel foam both came from MTI Corporation. The microwave used was a standard commercial Rival 1050W device purchased from a commercial retailer. All water utilized came from a Synergy water purification system by Millipore conditioned to 18.2 MΩ water.

3.2.2 Microwave-Assisted Synthesis of Electrocatalysts

The FeNi catalyst was synthesized using a sol-gel method analogous to a previously reported process with slight modifications.[89] Succinctly, the salts were combined with 0.02 mol of the metal ion and dissolved in water for a 100 mL total volume. Apart, 1.99 grams of sodium bicarbonate was dissolved in water for a 100 mL total volume. Solutions were treated with ultrasonication to fully dissolve. The sodium bicarbonate was used to titrate the metal solution at a 2.5-3mL/min rate while stirring for a total titration time of ca. 45 minutes. The suspensions underwent gradual color changes throughout the titration. After titration the suspension remained stirring for one hour. The suspension was then transferred to Nalgene bottles and placed in the microwave for approximately two minutes while stopping to swirl every 15 seconds. As the suspension was microwaved, it formed bubbles as it boiled from the bottom and up the sides of the bottles. This general procedure was repeated for each combination of metals adjusting only the weight amounts for the desired percentage within the suspension.

3.2.3 Electrode Fabrication

The mixed metal oxide nanoamorphous suspensions were coated onto the three supports (nickel foam, carbon weave, and FTO) by electrodeposition using a CHI potentiostat. For support preparation the FTO was rinsed with soap, water, and ethanol before being treated with ultrasonication in ethanol for 15 minutes then taken out to air dry for five minutes then immediately deposited upon. The carbon weave was fired in air at 300℃ for 3 hours with a 1°C min^{-1} ramp rate. The nickel foam required no pre-treatment prior to electrodepositing. For eletrophoretic deposition, the supports were placed into a customized Teflon cell with holders for a reference electrode (sat Ag/AgCl) and disk counter electrode (titanium). Electrophoretic deposition was achieved in a three electrode system by applying a -1.1V potential to the working electrode for 10 minutes.

3.2.4 Electrochemical Measurements

All electrochemical data were collected using a CH Instruments potentiostat. Each experiment was performed in a customized Teflon cell with a Ag/AgCl (sat KCl) reference electrode and a 200μm Pt wire counter electrode. Preliminary cyclic voltammograms shown in Figure 3.5 were conducted in 1M NaOH while all subsequent tests were performed in 3M NaOH as to be closer to industrial standards. All potentials were corrected for uncompensated resistance and overpotentials were calculated with respect to the normal hydrogen electrode (NHE) using Equation 3.1.

$$E_{\mathrm{NHE}} = E_{\mathrm{Ag/AgCl}} - E^0 + / - REshift \tag{3.1}$$

The working electrode sample area for the cyclic voltammograms in Figure 3.5 were 0.49cm^2 while all subsequent electrode areas were 0.07917cm^2, just normalized to geometric surface area. Cyclic voltammograms were used to evaluate the OER activity of the electrodes. Capacitance was determined by cyclic voltammetry sweeps in the nonfaradaic current range at scan rates of 800, 400, 200, 100, and 50 mV/s.

3.2.5 Material Characterization

The surface morphology of the electrocatalyst and foam support was obtained using a scanning electron microscope (SEM) FEI Versa 3D Dual Beam instrument. For the atomic structure, a

FEI Tecnai F20 XT Field Emission Transmission Electron Microscope (TEM) was used to obtain images and electron diffractograms of the atomic structure at high-resolution. X-ray photoelectron spectroscopy (XPS) spectra were recorded using a PHI 5000 VersaProbe II X-ray Photoelectron spectrometer that used a monochromatic Al X-ray source. The adventitious carbon 1s binding energy to calibrate the binding energy scale was 284.8 eV.[104] Spectra were analyzed through the software CasaXPS.

3.3 Results and Discussion

3.3.1 Amorphous Electrocatalysts Synthesis and Characterization

A challenge in synthesizing homogeneously-dispersed mixed-metal oxides is avoiding segregation of the individual oxides. With the microwave-assisted synthesis technique that we have previously described,[29,102] metal nitrate salts are HR-TEM images of the FeNi and the FeNiCo electrocatalysts deposited on a carbon grid are shown in Figure 3.1. From a scale of 100 nm down to 5 nm the HR-TEM images do not show any crystalline structure. This assertion is further supported by the ring structure and lack of diffracted spots in the electron diffractograms Figure 3.1 inlays. These results are indicative that the microwave-assisted synthesis yields a nanoamorphous network of particles and even more encouraging as scaled from dual to triple metal combinations.

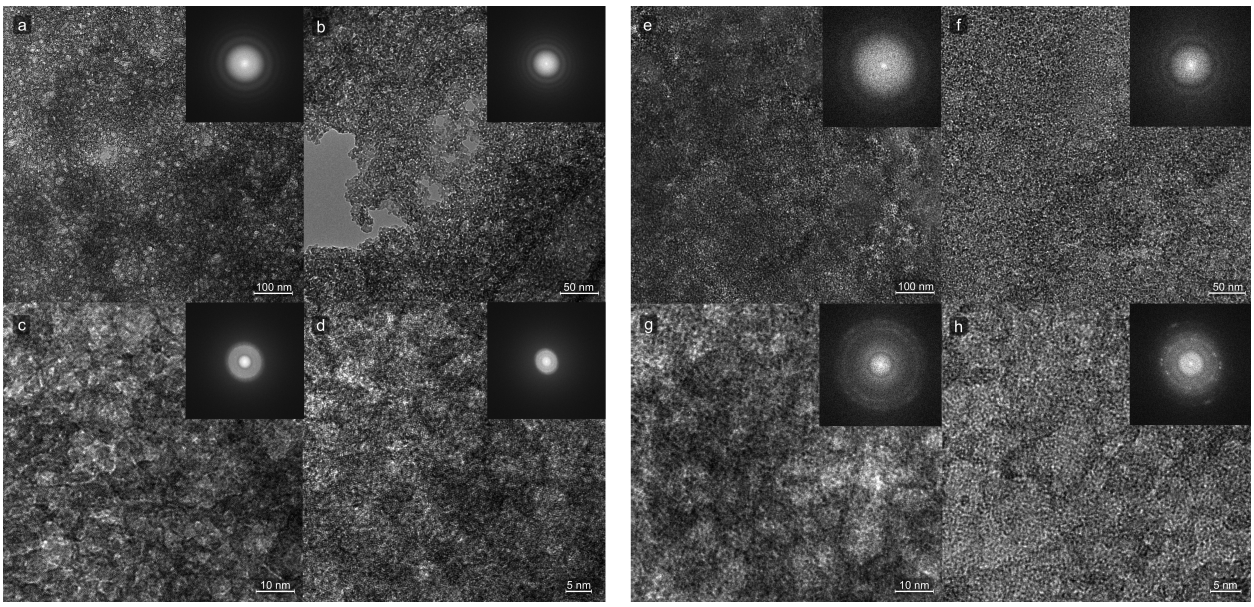

Figure 3.1. HR-TEM images of FeNi (left) and FeNiCo (right).

SEM images of the plain nickel foam are shown in Figure 3.2 as a baseline for comparing the coated nickel foam. The plain nickel foam structure and surface morphology can be seen in the top two images. The bottom row shows the FeNi electrocatalyst electrodeposited on the nickel foam with no extra treatment. The images show a uniform coating with homogeneous sized particles of ca. 250 nm which is the expected morphology for the microwave-assisted synthesis method. Also these images present no iron segregation even though the iron content is above 25%.

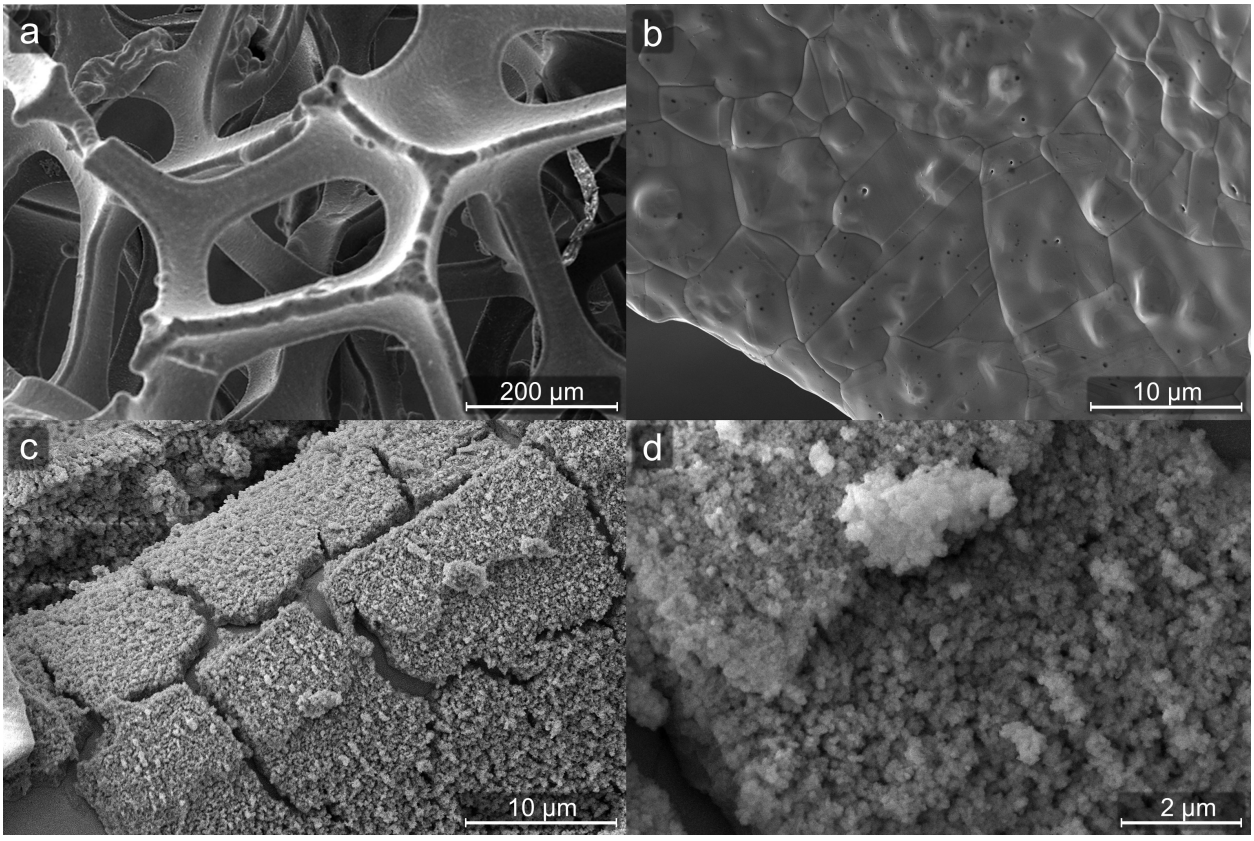

Figure 3.2. SEM images of plain nickel foam (a&b) and FeNi electrodeposited nickel foam (c&d).

3.3.2 X-ray Photoelectron Spectrometry Results

The XPS analysis performed on the FeNi coated nickel foam show both iron and nickel oxides and oxyhydroxides. For oxygen, there are two separate peaks at 529.9eV and 531.6eV which are consistent with FeNi oxide and oxyhydroxides respectively (or structural defects of either).[105,106] The Ni 2p core level binding energies at 855.7eV and 861.6eV are consistent with those reported for nickel oxy(hydroxides) and iron nickel oxide.[107–109] The Fe 2p core level binding energies and

spectral shapes for iron oxides and hydroxides like FeO, Fe_2O_3, Fe_3O_4, FeOOH, and in $FeNiO_4$ are too similar to distinguish between.[110–112] Based on the spectra for the oxygen and nickel it can be assumed the iron peaks correspond to iron nickel oxide and iron oxy(hydroxide). These results are shown in Figure 3.3.

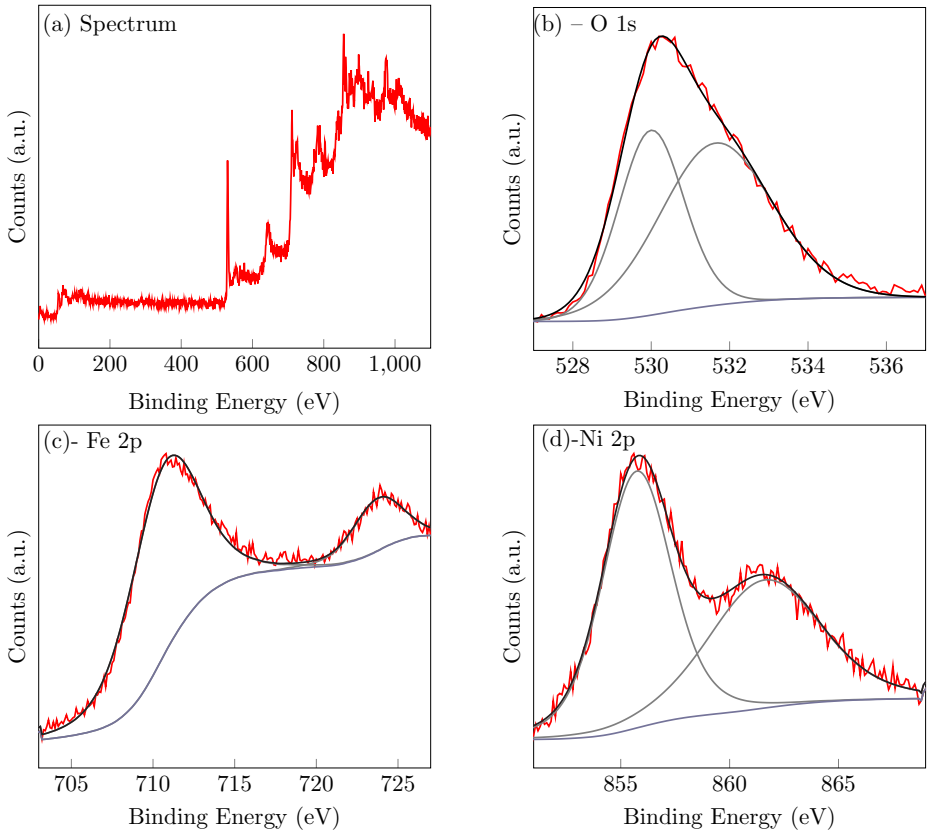

Figure 3.3. X-ray photoelectron spectroscopy of the microwave-assisted FeNi on Ni foam support.

3.3.3 Capacitance Measurement Results

Double layer capacitance measurements, C_{dl}, were performed via cyclic voltammetry (CV) to demonstrate the large increase in electrochemical surface area (ESCA) by using high surface area supports. These results are shown in Figure 3.4 where the data were collected in the nonfaradaic current region for each sample. The current in this region is proportional to the scan rate and the electrochemically active surface area of an electrode as depicted in Equation 3.2[113]

$$i = C_{\mathrm{dl}} * scanrate(dv/dt) \tag{3.2}$$

Using this relationship, the dependence of the current on the scan rate produces a linear trend which is consistent with capacitive charging behavior seen in Figure 3.4. The slope of these lines divided by the geometric surface area yields the ESCA for each corresponding electrode.

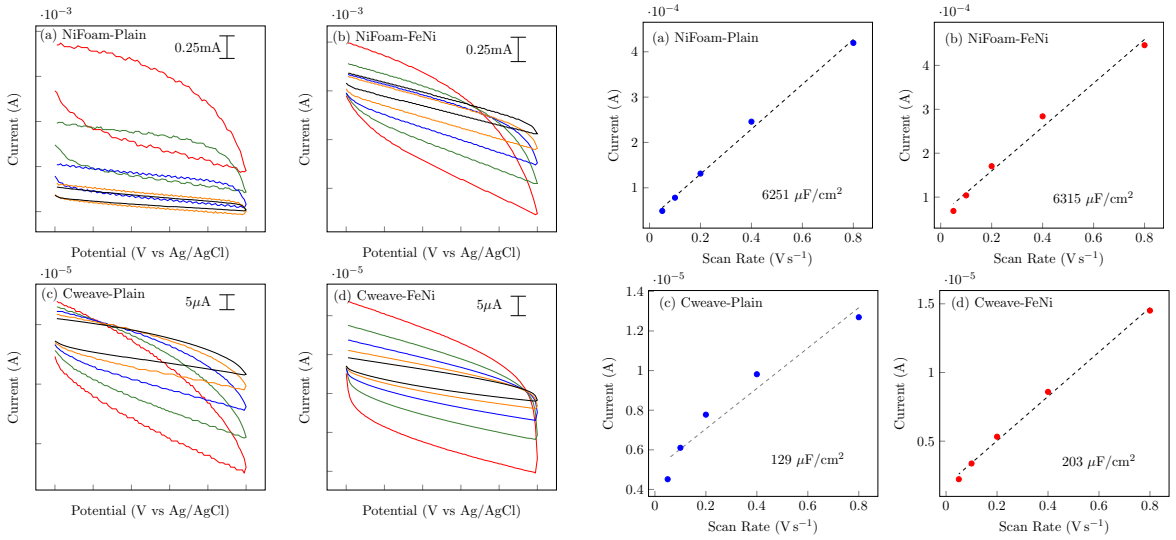

Figure 3.4. Double-layer capacitance measurements via cyclic voltammetry in 3M NaOH on plain Ni foam (a-left) electrodeposted FeNi on Ni foam (b-left) plain C weave (c-left) and electrodeposited FeNi on C weave (d-left). On the right are the corresponding regression lines.

As previously stated, double layer capacitance measurements can be unreliable for most nickel-iron systems[29,93,102,114] and inaccurate due to the insulating nature of nickel.[115] Therefore, the recorded ESCA often reflects the underlying support rather than the catalyst itself. In the beginning, for the cyclic voltammograms shown in Figure 3.5 the tests were conducted on FTO. A previously reported value for FTO glass capacitance is approximately 12μF cm^{-2}.[29,102] As shown in Figure 3.4 the ESCA value for plain carbon at 129μF cm^{-2} is 10x increase in magnitude from the plain FTO capacitance. Even more, the nickel foam possess in ESCA a magnitude 100x that of FTO and 10x that of plain carbon for a capacitance value of 6251μF cm^{-2}. Between the coated and uncoated results, a slight increase can be seen for both supports. In this case, ESCA makes it clear the performance difference between the supports FTO, carbon weave, and nickel foam can be attributed to the variation in ESCA as well as showing a small increase in ESCA, ca. 65-75μF cm^{-2}, for the support coated with the FeNi electrocatalyst compared to the plain supports.

3.3.4 Electrochemical Cyclic Voltammetry Results

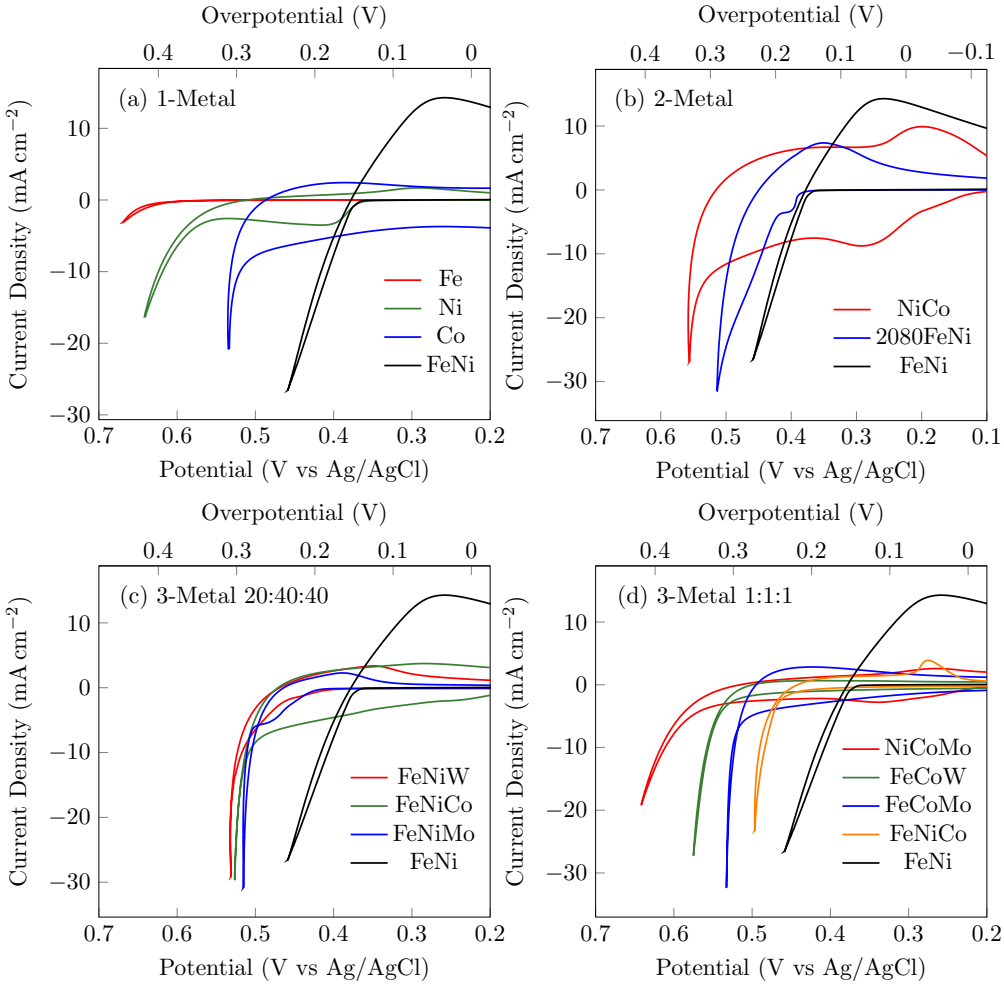

Figure 3.5. Cyclic voltammograms of microwave-assisted multi-metal catalysts coated on fluorine doped tin oxide (FTO) glass tested in 1M NaOH at 50mV s^{-1} and corrected for uncompensated resistance (R_u).

Cyclic voltammetry was used to differentiate the OER activities between the various mixed metal combinations tested. Using the facile microwave synthesis, we produced a variety of combinations in search of an electrocatalyst superior to that of our previous $Fe_{0.2}Ni_{0.8}$ electrocatalyst. Shown in Figure 3.5 are the single metals, double metals, and ternary metals we synthesized and tested. For the ternary metals we explored combinations with the lower 20% iron in the case of possible segregation. With the result from the FeNi, we also tried combinations containing more than 20% iron in equivalent ratios. To clearly demonstrate the performance of all combinations and readily correlate all results we have included the champion combination FeNi on each plot within Figure 3.5.

When evaluating OER performance, the benchmark widely accepted is 10 mA cm^2 in order to compare and evaluate electrocatalytic activity. This metric significance stems from solar hydrogen production.[14,116] Additionally, a large redox curve denoted on the return sweep for the FeNi scan correlates to activity.[117] Using these two assessments, the FeNi electrocatalyst performed the best for the OER with an overpotential of at 10 mA cm^2. After determining the FeNi to be the best OER electrocatalyst, we sought to further improve performance by depositing on a porous, high surface area supports.

Cyclic voltammetry was also used to evaluate the OER performance using FeNi on the carbon weave and nickel foam supports. Compared in Figure Figure 3.6a are the activities of the plain supports compared to the coated supports. It can be seen the addition of the FeNi electrocatalyst increased performance for both the carbon weave and nickel foam supports. Additionally, the nickel foam outperformed the carbon weave both coated and uncoated. As seen in the SEM images, the open network of the nickel foam allows for the electrocatalyst to both increase in available surface area compared to the FTO but also space for oxygen to diffuse out. Due to the dense nature of the carbon weave paper, the likely limiting factor for OER performance is product site blocking.

The overpotential shown in figure Figure 3.6a obtained by cyclic voltammetry in figure Figure 3.6c is fairly close to steady-state. At a scan rate of 2mV/s, the system is close to overcoming the transient concentration gradients that are typical with faster scan rates. In order to confirm steady-state conditions, the overpotential was determined by benchmarking the OER catalytic activity as described by Jaramillo. As seen in Figure 3.6b the steady-state overpotentials at 30 s from the chronopotentiometry experiments and the steady-state currents at 30 s from the chronoamperometry experiments fit well the cyclic voltammetry data denoted by the circles, squares, and solid line respectively. Finally, to further investigate both the steady-state as well as the stability of the FeNi electrocatalyst on the nickel foam, a two hour chronopotentiometry at both 10 mA cm^{-2} and 100 mA cm^{-2} were performed. These results were all in close agreement with overpotentials of 345mV, 194 mV, 204 mV for the cyclic voltammogram, 30 s chronopotenitometry, and two hour chronopotentiometry experiments respectively.

3.4 Conclusions

In this work we have improved upon performance for an electrocatalyst used for half reaction OER in water splitting. Executing a previously developed synthesis method, additional multimetal nanoamorphous electrocatalysts were fabricated in order to yield competitive activity. This champion combination, FeNi, was then further enhanced by electrodepositing onto a high surface area support, nickel foam. The catalyst herein provides an overpotential of ca. 200 mV at 10 mA cm^{-2} on the nickel foam. This modest development will aid in the implementation of an alkaline water electrolysis device. This advancement can ultimately help in the production of hydrogen as an alternative fuel source relieving current strain on environment and nonrenewable resources.

3.5 Acknowledgement of Contributions

SEM images were obtained with help from Dr. Prem Thapa and Dylan Jantz.

3.6 Supporting Information

The following figures, Figure 3.7 to Figure 3.10 , are additional data gathered in pursuit of the FeNi on nickel foam electrocatalyst development. Another experiment conducted for this project explored the possibility of concentrating the nanoparticle suspension by removing excess water from the precursors. This was attempted through both desiccation as well as through a schlenk line process. Unfortunately, unlike Figure 3.8 and Figure 3.9 these results were inconsistent. Also scanning electrochemical microscopy (SECM) tests were conducted for the ternary FeNiCo in hopes of obtaining insights into the kinetics of the active sites. Similarly, for Chapter 2 HER electrocatalyst development, SECM tests were done but these also were producing unusual results. A continuation on these anomalies created a new side project pursued by another student.

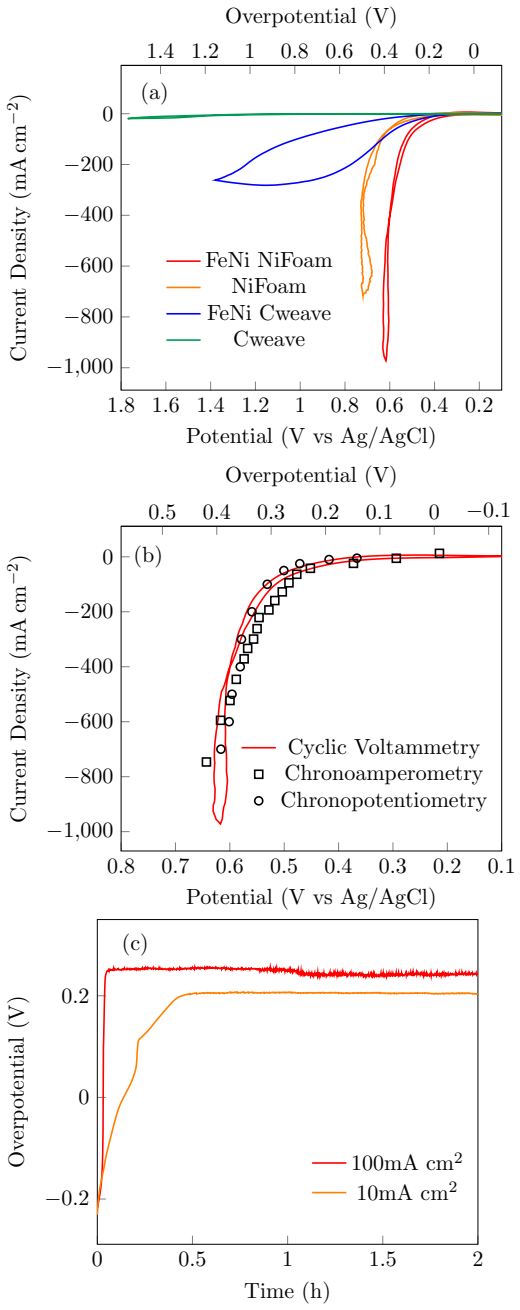

Figure 3.6. (a) Cyclic voltammograms of nickel foam and woven carbon supports plain and with microwave-assisted catalyst FeNi electrodeposited tested at 2mV s^{-1} (b) Cyclic voltammogram at 2mV s^{-1} with chronoamperometry experiements at 30s for steady-state currents (squares) and chronopotentiometry experiments at 30s for steady-state potentials (circles) all on microwave-assisted FeNi on NiFoam (c) Chronopotentiometry experiments on FeNi electrodeposited NiFoam at 100mA cm^2 and 10mA cm^2 for 2 hours. All experiments performed in 3M NaOH and corrected for uncompensated resistance (R_u).

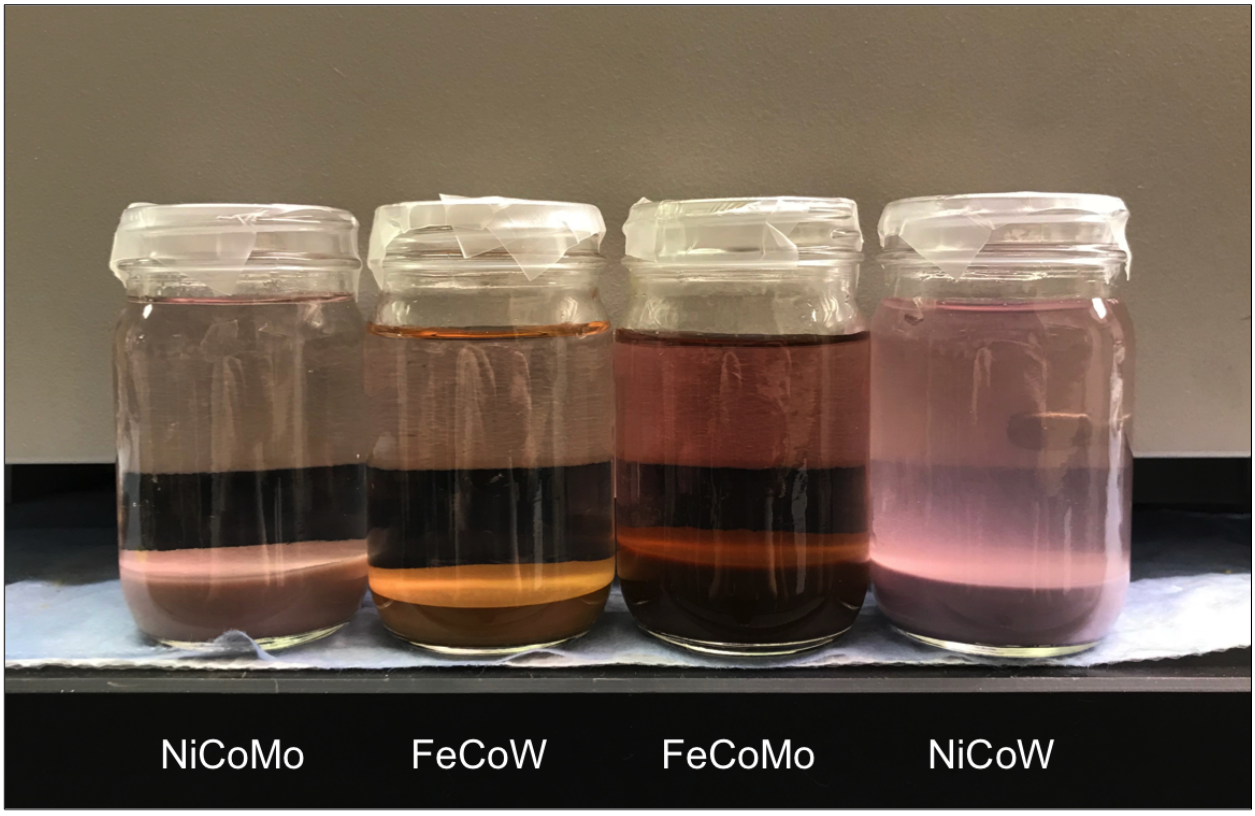

Figure 3.7. Nanoamorphous mixed metal oxides in solution after the microwave-assisted heating step in 125 mL Nalgene bottles then transferred to glass jars for long-term storage.

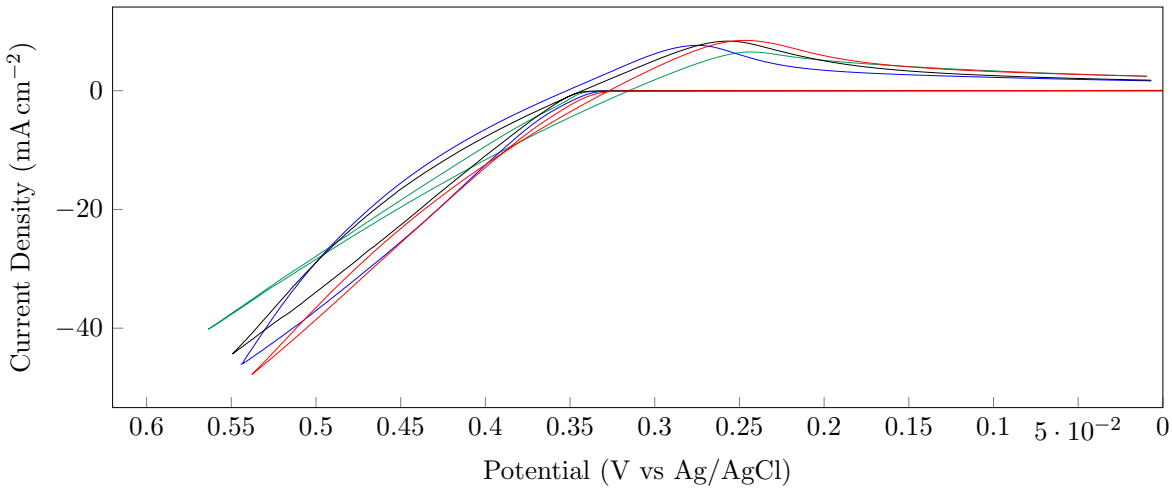

Figure 3.8. Different FeNi on FTO samples scanned at the same conditions to depict reproducibility.

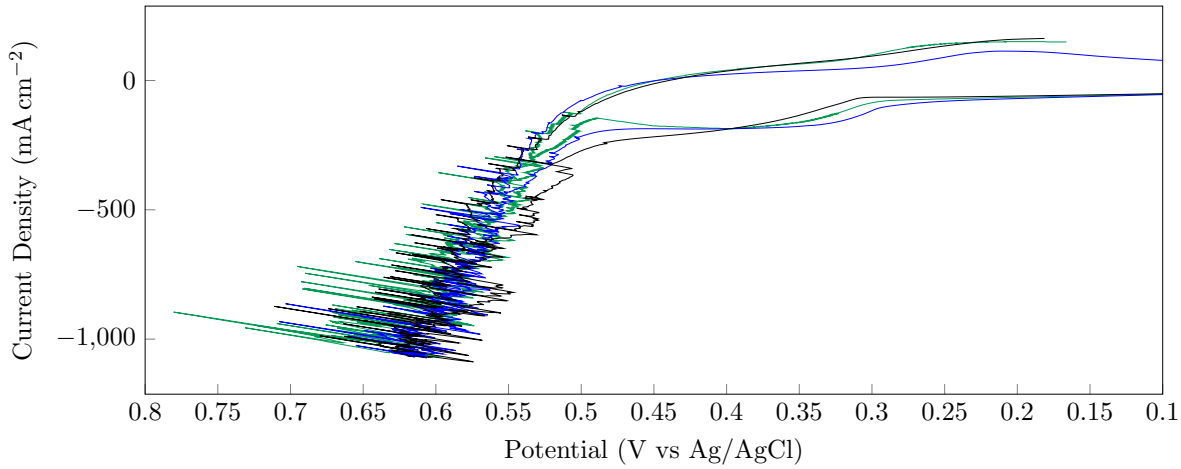

Figure 3.9. Different FeNi on nickel foam samples scanned at the same conditions to demonstrate reproducibility.

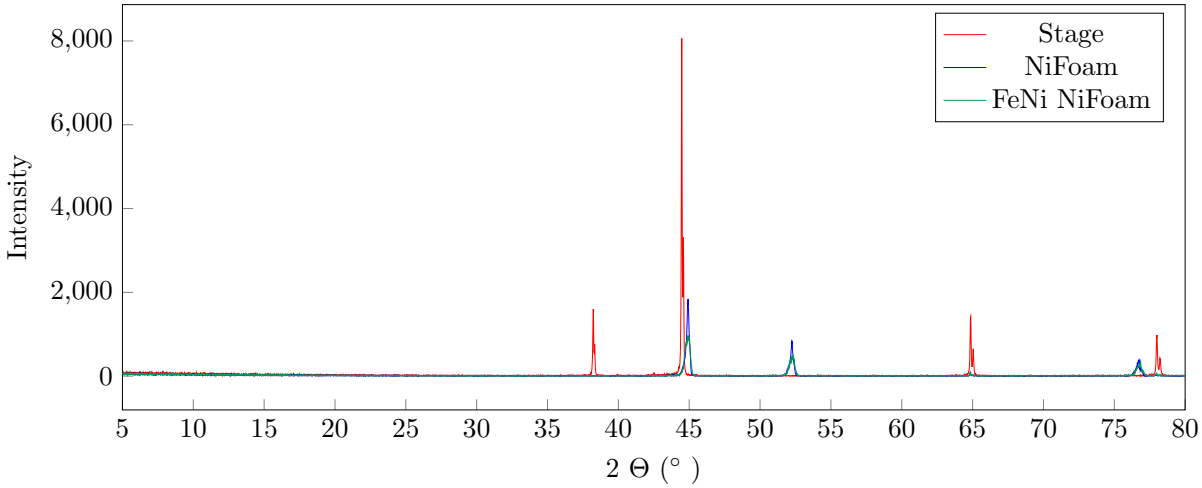

Figure 3.10. X-ray diffraction scans on the microwave-assisted FeNi on Ni foam support, plain Ni foam support and the XRD stand to confirm coating present on Ni foam.

Chapter 4

Nanoamorphous $Co_{0.8}$:$Ni_{0.2}$ Electrocatalyst on Porous, High Surface Area Nickel Foam for Hydrogen Evolution Reaction

4.1 Introduction

There is significant interest in alternative energy sources that are sustainable for infinite use as well as for the earth. This interest has becoming increasingly vital as global usage surges and the current fossil fuel supply is diminishing.[118] Hydrogen has emerged as a promising alternative among the recent research into replacing fossil fuels. It has gained support due to its high efficiency, zero emissions in fuel cell electric vehicles, and ability to be produced domestically.[119] One of the current drawbacks for using hydrogen as an "environmentally" beneficial fuel source is the production method. The main production method for hydrogen is through steam reformation. This process produces carbon dioxide and other emissions countermanding the goal of reducing environmental impacts. An alternative to producing hydrogen is water electrolysis, which uses electricity to split water into hydrogen and oxygen.[120] By using renewable energy sources such as solar, wind, biomass, geothermal, and hydroelectric, this process can be further improved. Water

electrolysis is also a facile way to produce high purity, ca. 99.8%, hydrogen with a quick start up time. The most common and promising electrolyzer is an alkaline for the substantial efficiency and lower cost compared to other types.[94,95]

One of the challenges associated with hydrogen production via water electrolysis is the energy requirement. While conducting research for the oxygen evolution reaction, OER, we considered applying similar techniques to improve performance and decrease the energy usage for the hydrogen evolution reaction, HER. Using the microwave-assisted synthesis route, a variety of combinations based on literature search and prior research for OER were produced. The idea being to focus on non-noble metals that have already shown promise as well as materials that could potentially work for both OER and HER.

Grand challenges for hydrogen evolution reaction catalysts are very similar to the oxygen evolution reaction challenges. Mostly catalysts aim to be low in cost, abundant, and highly active for selective products. Unfortunately one of the most active catalysts found to date for HER, platinum only fits one of those criteria as it is both expensive and very limited in quantity.[118,121] Recent research into the metals Mo, Co,and Ni guided the choice to test those three metals in this paper.[121–124]

This work attempts to find a widely available, low cost, and active electrocatalyst for the hydrogen evolution reaction. It will use a previously disclosed microwave-assisted synthesis route to produce different nanoamorphous mixed metal oxide electrocatalysts to find the most active for HER. This catalyst will then be deposited onto a high surface area support to further improve performance. Finally we will demonstrate this electrocatalyst, supported and understood by characterization techniques, improves upon other literature search for a HER electrocatalyst to use in water electrolysis.

4.2 Experimental

4.2.1 Materials

Iron (III) nitrate nonahydrate (98%+, ACS Reagent, Acros), nickel (II) nitrate hexahydrate (99%, Fisher Scientific), cobalt (II) nitrate hexahydrate (98%+, ACS Reagent, Acros), ammonium molybdate (VI) tetrahydrate (ACS Reagent, Acros), sodium hydroxide (Fisher Chemical), and

sodium bicarbonate (Tech, Fisher Science Education) were used as without any modifications. Aldrich Chemistry supplied the glass slides coated with fluorine doped tin oxide (FTO) at ca. 7Ω surface resistivity. Nickel foam was provided by the MTI Corporation. A standard commercial Rival 1050W microwave device was purchased from a commercial retailer. The water used for all experiments was purified using a Millipore system conditioned to 18.2 MΩ water.

4.2.2 Microwave-Assisted Synthesis of Electrocatalysts

All catalysts were produced utilizing an established sol-gel method that has been formerly disclosed.[89] In short, the salts were added in quantities of 0.02 mol of the metal ion and dispersed in water with a total volume of 100mL. Independently, 1.99g of sodium bicarbonate was dispersed in a total 100mL volume with water. Any solutions that did not dissolved were sonicated. Sodium bicarbonate, was dropped at a rate of about 2.5-3mL per minute into the metal solution for a total titration time of ca. 45 minutes. During this time, the suspension was continuously stirred. Suspensions were observed to undergo gradual color changes. At the end of titration, suspension stirred for one hour. At the end of the hour, the suspension was poured into Nalgene bottles and microwaved for about two minutes. Every 15 seconds, the suspension was swirled to mix. Suspension at the end of microwaving would exhibit bubbles on sides of bottles as well as bubbles rising from the bottom. This procedure was analogous for the corresponding metal salt combinations.

4.2.3 Electrode Fabrication

The various metal oxide suspensions were electrodeposited using a CH Instruments potentiostat onto all two different supports. The two different supports used were FTO and nickel foam. The FTO was first rinsed with soap, water, and ethanol then sonicated in a beaker of ethanol for approximately 15 minutes. After which each piece was removed only touching the sides to place on a Kimwipe to air dry then promptly coated as to avoid excess dust/dirt from the air to adhere to the glass. The nickel foam was used as received without any conditioning. For the electrophoretic deposition, the supports were held within a specialized Teflon cell containing troughs for suspension, reference electrode, and counter disk electrode. Depositing conditions were to apply a -1.1V potential for 10 minutes in a three electrode system.

4.2.4 Electrochemical Measurements

The electrochemical experiments were conducted using a CH Instruments potentiostat. The tests were completed in a customized Teflon cell using a Ag/AgCl saturated in KCl reference electrode and for the counter electrode a 200μ Pt wire. Initial cyclic voltammetry data is represented in Figure 4.4 where these tests were performed using 1M NaOH. All other data was carried out in 3 M NaOH in order to closely replicate industrial conditions. Altogether, all data was corrected for uncompensated resistance. Overpotential calculations were performed according to Equation 3.1 in regards to the normal hydrogen electrode (NHE). The area used for the working electrode was determined by the usage of o-rings, and was 0.49cm^2 in Figure 4.4 while all subsequent electrode areas were 0.07917cm^2. The cyclic voltammograms were utilized in order to find the reactivity of the HER electrocatalysts. The cyclic voltammograms were also used to determine the capacitance by sweeping in the nonfaradaic current region at the scan rates 800, 400, 200, 100, and 50 mV/s.

4.2.5 Material Characterization

Scanning electron microscopy (SEM) was the technique used in order to determine the surface morphology of the electrocatalyst. The SEM instrument was a FEI Versa 2D Dual Beam. A PHI 5000 VersaProbe II X-ray Photoelectron spectrometer instrument that utilzed a monochromatic Al X-ray source collected the x-ray photoelectron spectroscopy (XPS) spectra data. In these cases an adventitious carbon 1s binding energy of 284.8 eV was used to calibrate.[104] These specra were analyzed by the CasaXPS software.

4.3 Results and Discussion

4.3.1 Amorphous Electrocatalyst Synthesis and Characterization

Prior research into synthesizing homogeneously-dispersed mixed-metal oxides while avoiding segregation of the individual oxides was successful in two distinct papers reported by our group.[29,102] These articles provide evidence given by HR-TEM for the amorphous quality of the electrocatalysts. Additionally, HR-TEM confirmed approximate size of the network of nanoparticles present using this method. Those same methods used for suspension fabrication were implemented in this study.

4.3.2 X-ray Photoelectron Spectrometry Results

XPS spectra on the champion electrocatalyst, $Co_{0.8}$:$Ni_{0.2}$ deposited on nickel foam, is shown in Figure 4.1. These results are indicative of a cobalt nickel oxide.[125–127] For oxygen there is only one peak suggesting a homogeneously dispersed catalyst. The Co 2p core level binding energies are located at 769eV, 776.5 eV, and 783.5eV. The Ni 2p core level binding energies are shown at 851.5eV and 858eV. These closely match values reported in literature for metal oxides however there is a slight shift even after normalizing to 284.8eV adventitious carbon.[128] These results can be seen in Figure 4.1

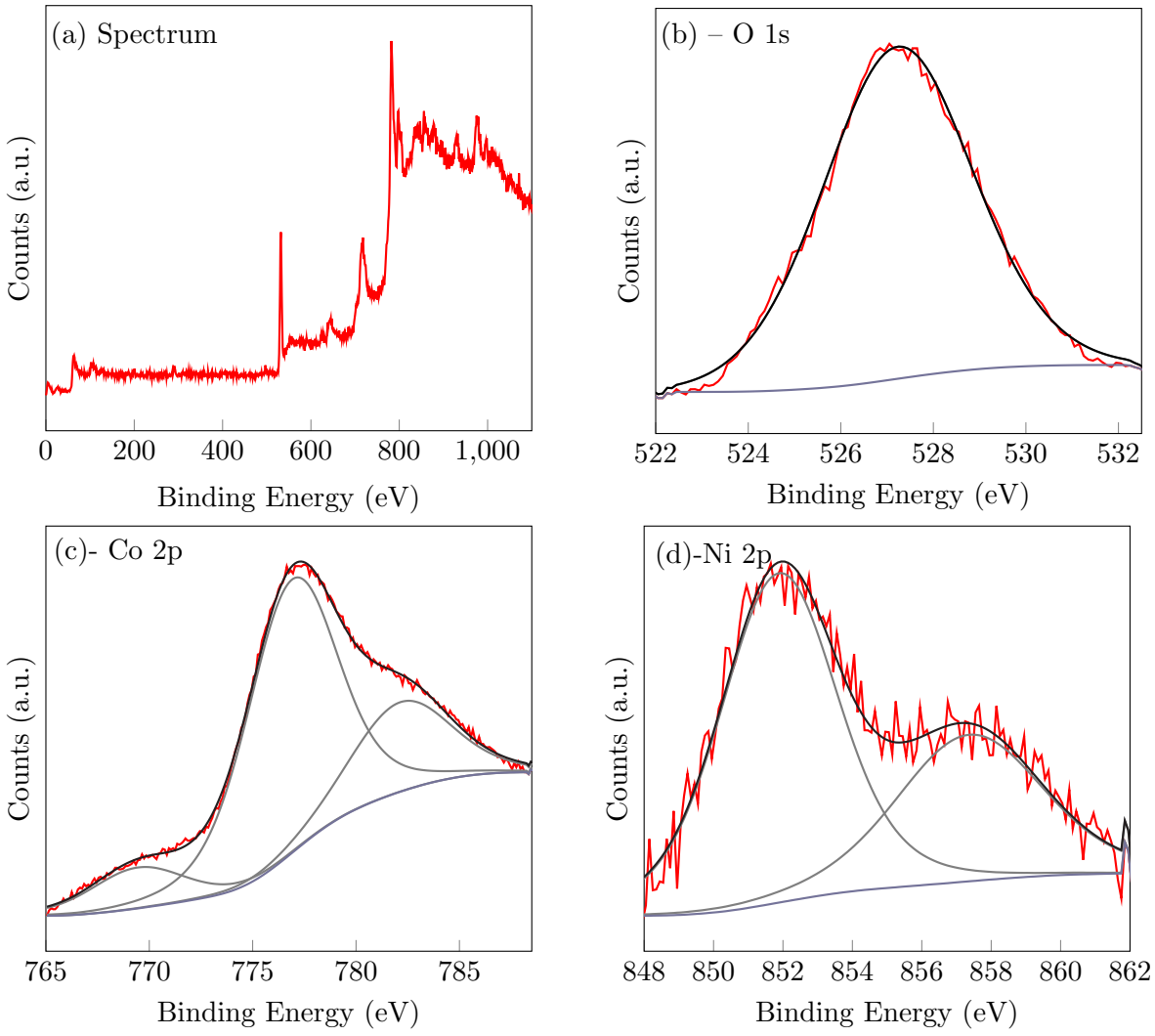

Figure 4.1. X-ray photoelectron spectroscopy of the microwave-assisted $Co_{0.8}$:$Ni_{0.2}$ on Ni foam support

Meanwhile, the SEM images of the coated and plain supports are shown in Figure 4.2. These images both verify a coating is present as well as yielding insight into the surface morphology important to electrocatalysis activity. The top images show the pain nickel foam at different magnifications. The bottom images are of the $Co_{0.8}$:$Ni_{0.2}$ electrodeposited on the nickel foam. These images exhibit uniform particle sizes of ca.

nm and homogeneously dispersed on the network of nickel foam. This is the predicted result of using the microwave-assisted synthesis. It has been suggested that a current electrocatalyst design objective is obtaining a high surface area of nanoamporphous particles which would have the potential to greatly improve performance.[34] As supported by the nickel foam, helping to increase surface area, the suspension successfully deposited evenly and maintained the nanoparticle size and amorphous structure.

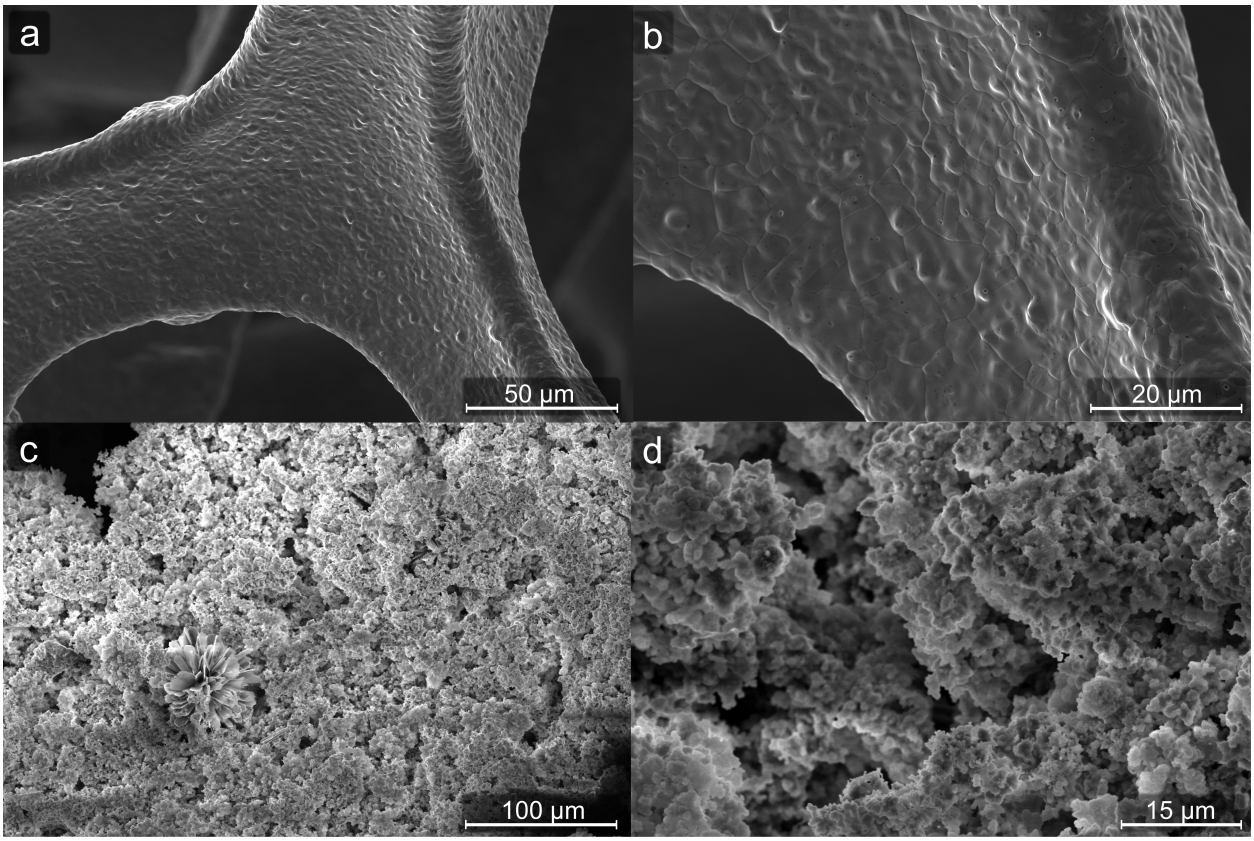

Figure 4.2. SEM images of plain nickel foam (a&b) and $Co_{0.8}$:$Ni_{0.2}$ electrodeposited nickel foam (c&d).

4.3.3 Capacitance Measurement Results

Cyclic voltammetry was used to explore the electrochemical surface area (ESCA) using the high area supports. These measurements are called double layer capacitance, C_{dl}. The results displayed in Figure 4.3 were tested in the nonfaradaic current region. This was determined by running a cyclic voltammogram out to upper and lower voltage ranges. By using the nonfaradaic region, the current will be directly proportional to the scan rate and the electrochemically active surface area of the electrode as described by Equation 3.2.[113] This relationship determines the dependence of the current on the scan rate which should be linear. As seen in Figure 4.3 the trend produces a linear correlation that is expected for capacitive charging behavior. The slope of the lines is divided by the geometric surface area in order to obtain the ESCA value for each electrode.

The results in Figure 4.4 were performed on FTO. Prior reporting for capacitance on FTO is about 12μF cm^{-2}.[29,102] The high surface area support nickel foam is 400x the capacitance of FTO with a value of 4836 μF cm^{-2}. This supports the claim that increasing ESCA helps to increase the performance of an active electrocatalyst. Furthermore, the low difference between the plain nickel foam and coated nickel foam can be attributed to the insulating nature of nickel as described in literature.[115]

4.3.4 Electrochemical Cyclic Voltammetry Results

A variation of mixed-metal oxides were synthesized using the microwaved-assisted synthesis. In order to evaluate the performance of the different mixed-metal oxides, the cyclic voltammetry technique was used. The results of these tests are shown in Figure 4.4. They show the difference in activity between single, double, and double 80:20 metals and high surface area supports as well as a platinum disk, a reported high performing HER catalyst. To compare activity between the electrocatalysts, a benchmark of about 10 mA cm^2 was chosen to obtain an overpotential value.[14,116] The lower the overpotential the better the catalyst performs. At this stage, $Co_{0.8}$:$Ni_{0.2}$ was found to have the highest performance for HER and therefore was selected to test on a higher surface area support.

To evaluate HER performance on $Co_{0.8}$:$Ni_{0.2}$ deposited on nickel foam, cyclic voltammetry was used again. Compared in Figure 4.5 are the results of testing plain nickel foam and $Co_{0.8}$:$Ni_{0.2}$

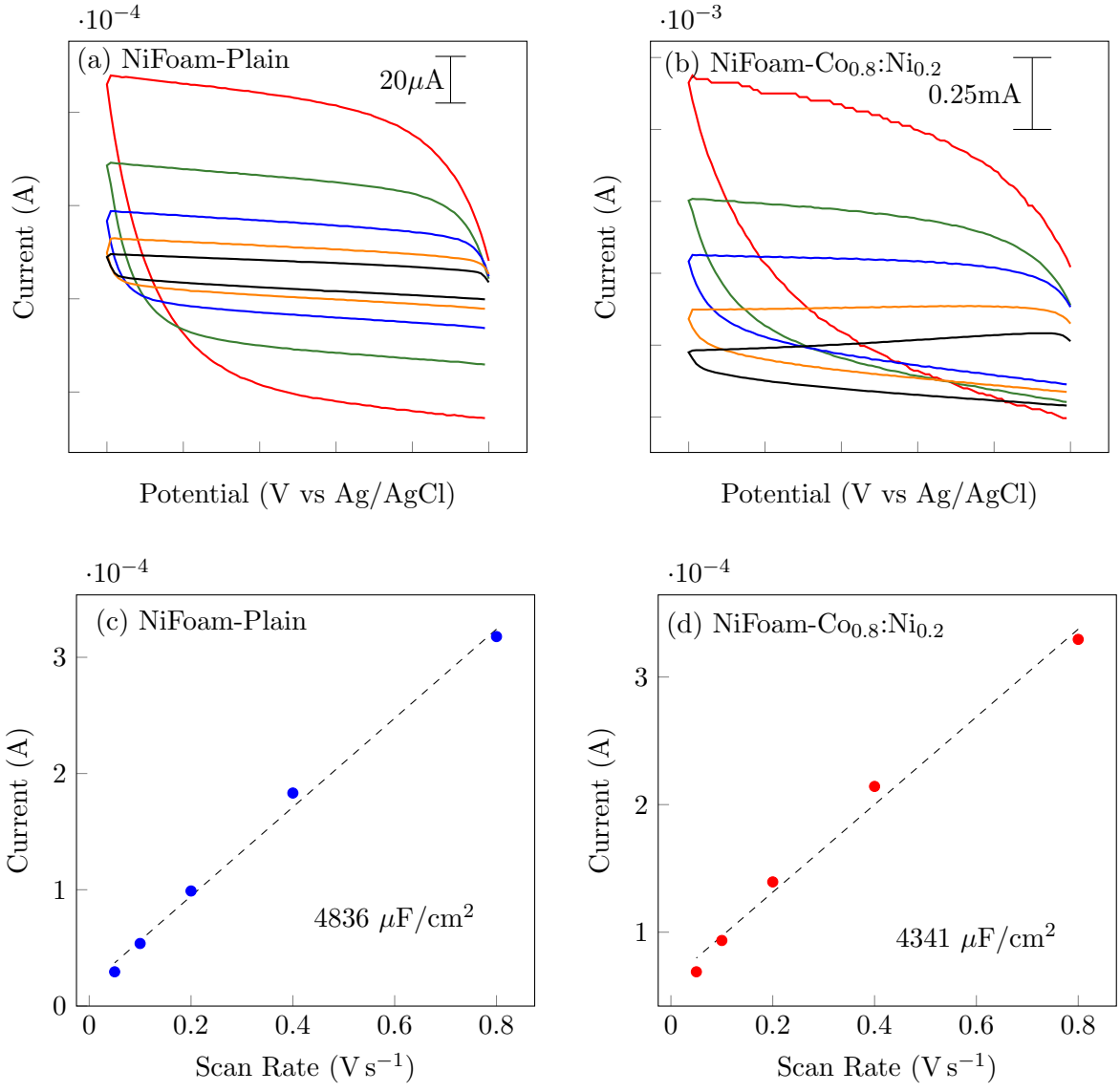

Figure 4.3. Double-layer capacitance measurements via cyclic voltammetry in 3M NaOH on plain Ni foam (a) electrodeposted $Co_{0.8}$:$Ni_{0.2}$ on Ni foam and double layer capacitance regression lines of Ni foam c and electrodeposited $Co_{0.8}$:$Ni_{0.2}$ (d).

coated nickel foam. As seen, the high surface area as well as adding the electrocatalyst improves performance. The higher surface area allows for more sites available and the network structure of the foam likely allows for more oxygen to diffuse out. These results are at a slow scan rate of 2mV s^{-1}. The overpotential obtained by cyclic voltammetry in Figure 4.5a is fairly close to steady-state in Figure 4.5b. This illustrates the system has mostly overcome any transient effects, such as concentration gradients, that can occur with quicker scan rates. To verify that steady-state had been achieved, the overpotential was calculated based on a benchmarking practice detailed by Jaramillo.[93] The results of these benchmarking experiments are shown in Figure 4.5b where circles represent steady-state overpotentials at t = 30 s from the chronopotentiometry experiments and the squares denote steady-state currents at t = 30 s from the chronoamperometry experiments both of which fit the cyclic voltammetry data, solid line, well. Lastly, in order to determine the stability of the $Co_{0.8}$:$Ni_{0.2}$ electrocatalyst on nickel foam, a two hour chronopotentiometry at both 10 mA cm^{-2} and 100 mA cm^{-2} were performed. The results from the cyclic voltammogram, steady-state, and stability tests all gave similar overpotential values at 104mV, 119mV, and 122mV at 10 mA cm^{-2}.

4.4 Conclusions

Herein we explored applying a synthesis technique to fabricate HER electrocatalysts that was previously used to develop OER electrocatalysts. These preliminary results were successful in producing active HER electrocatalysts on a flat substrate. To further improve upon this activity, the champion mixed metal oxide combination, $Co_{0.8}$:$Ni_{0.2}$, was electrodeposited on nickel foam, a high surface area support. This electrode structure combined with increasing molarity from 1 M to 3 M NaOH produced favorable results of an approximate 120mV overpotential at 10 mA cm^{-2}. These results will be instrumental in achieving a feasible alkaline water electrolyzer to produce hydrogen.

4.5 Acknowledgement of Contributions

SEM data was obtained with the help of Dr. Prem Thapa and Dylan Jantz.

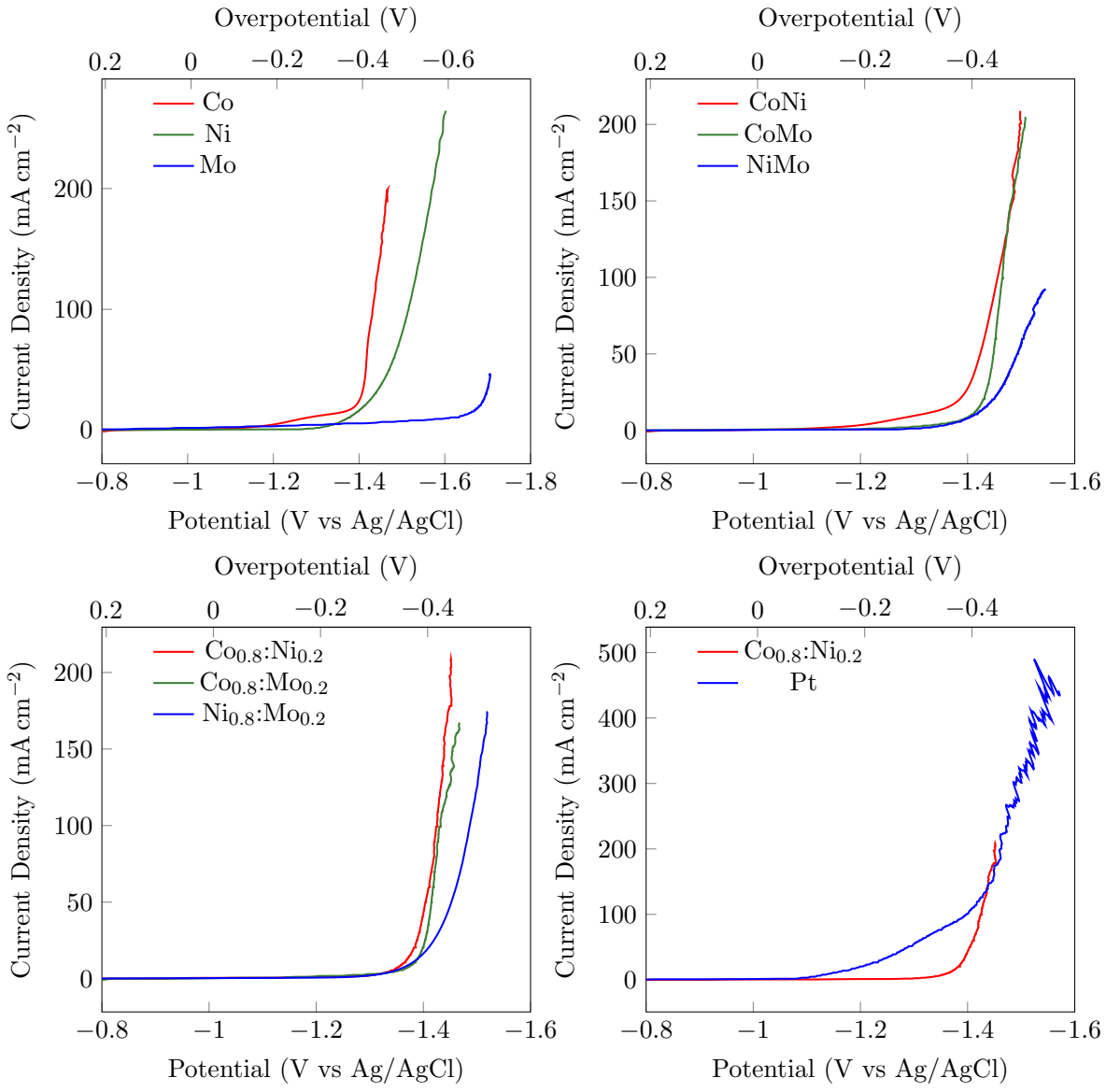

Figure 4.4. Cyclic voltammograms of microwave-assisted multi-metal catalysts coated on fluorine doped tin oxide (FTO) glass tested in 1M NaOH at 50mV s^{-1} and corrected for uncompensated resistance (R_u). (a-c) and the champion $Co_{0.8}$:$Ni_{0.2}$ compared with platinum disk electrode (d).

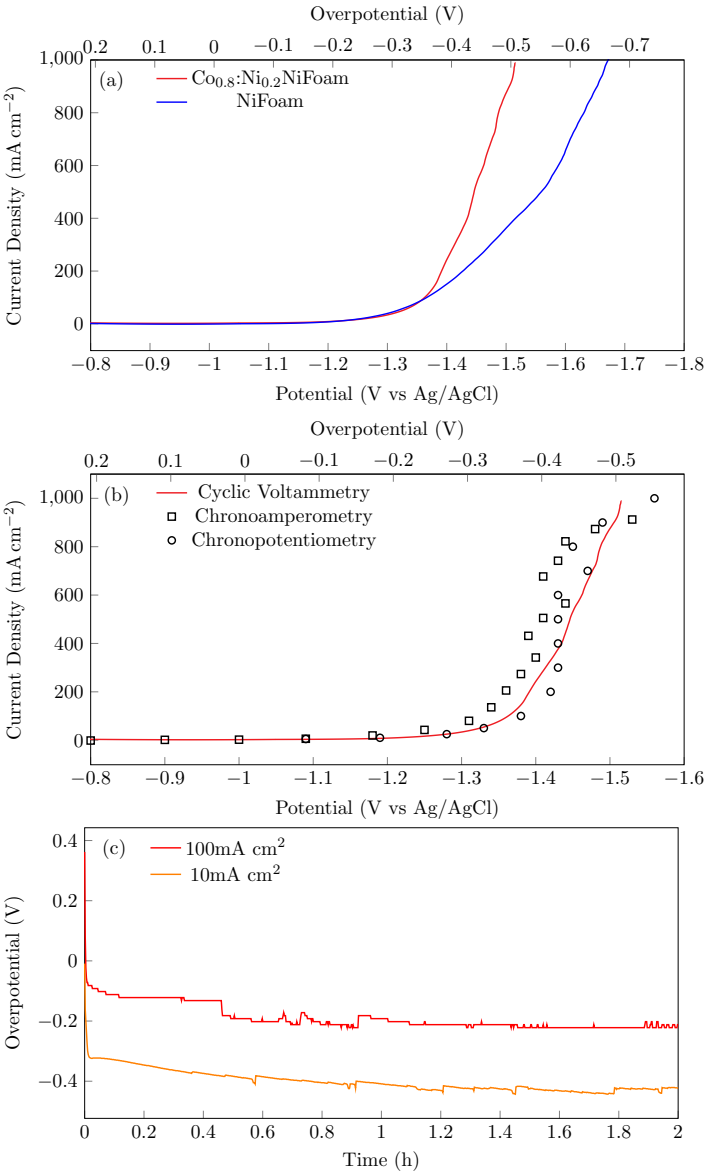

Figure 4.5. (a) Cyclic voltammograms of nickel foam with microwave-assisted catalyst $Co_{0.8}$:$Ni_{0.2}$ electrodeposited tested at 2mV s^{-1} (b) Cyclic voltammogram at 2mV s^{-1} with chronoamperometry experiements at 30s for steady-state currents (squares) and chronopotentiometry experiments at 30s for steady-state potentials (circles) all on microwave-assisted $Co_{0.8}$:$Ni_{0.2}$ on NiFoam (c) Chronopotentiometry experiments on $Co_{0.8}$:$Ni_{0.2}$ electrodeposited NiFoam at 100mA cm^2 and 10mA cm^2 for 2 hours. All experiments performed in 3M NaOH and corrected for uncompensated resistance (R_u).

Chapter 5

Conclusions and Future Work

5.1 Conclusions

Developing a sustainable process for producing hydrogen for use as an alternative fuel is of great research interest due to depleting energy sources and rising emissions effects. In order to implement a process such as water electrolysis, fundamental questions must be addressed. The topic of concern for the chapters presented in this work regarded promoting the water splitting half reactions, HER and OER, by way of electrocatalysis and process conditions. In order to begin to solve the main issues associated with this project, a few fundamental studies were conducted and are described in Chapter 1. The groundwork done in this section supported the subsequent chapters. A novel microwave-assisted synthesis technique was developed to fabricate mixed metal oxide nanoparticles. This simple technique started with metal salt precursors that after titrating formed metal carbonates and post microwaving decomposed to an amorphous oxide structure. This route takes approximately two and a half hours to complete and is only comprised of a basic chemistry procedure. Additionally, this first section addressed the mode of application of the electrocatalyst to the support. Ultimately, electrophoretic deposition yielded the best result for an even layer and superior performance,

Once the synthesis method was established, the main part of this project was to address the following concerns:

1. How will the synergistic effects of the multimetal catalysts effect performance and can they achieve a higher performance than current champion noble metals?

2. Is it possible to create 3D porous structures of highly active catalysts to increase active site densities and promote mass-transfer to and from the electrode surface?

It began with literature search to identify promising elements for the OER reaction. Once the precursors were chosen, the different combinations were fabricating using the developed microwave-assisted synthesis technique. The catalysts were systematically selected to be tested in combinations of 3 metals at equal ratios first. Then based on work by Bell and co-workers the ratios were adjusted in a 20:40:40 fashion in order to lessen potential iron segregation. However, we found that this did not have a large impact on performance as expected. This is likely the result from only one source of heating in a lower and more controlled manner than typical deposition. Additional studies were conducted to determine the best coating method between dropcasting and air drying, dropcasting and heating at 70℃ , UV lamp, dip-coated, and electrodeposited by applying a voltage for a certain length of time. Based on these results, electrodeposition provided the best consistent coverage and activity. Also experiments were completeed to ensure the optimal electrodeposition time and voltage were used. At this point, on FTO, $Fe_{0.2}$:$Ni_{0.8}$ synthesized by the microwave-assisted method yielded a low overpotential of 286 mV at 10 mA cm^{-2}.

To continue to build on this research, it was hypothesized that adding an additional active metal component to the synthesis may improve the activity of the electrocatalyst suspension. All preliminary tests were conducted on a flat fluorine-doped tin oxide glass slide in order to best see the difference in activity between the metal combinations. Using this catalyst, we then went on to explore the effect of using different supports. Most commonly used are carbon fiber substrates. However, considering the flow needed in an electrolyzer we wanted to look into something stronger that would last longer in the cell. For this we tried nickel foam. While the carbon paper marginally improved performance, the nickel foam greatly increased activity for the OER. We attributed this to the fact that its open structure allowed for better diffusion of reactants and products to the catalytic sites. Additionally, with the high surface area there are more sites available to participate. The FeNi electrocatalyst had the lowest overpotential of ca. 200 mV at 10 mA cm^{-2} and reached 1 A cm^{-2} on nickel foam. In addition to the use of a high surface area support, the operating conditions were improved from 1 M to 3 M NaOH.

Using the success from the OER electrocatalyst study, we applied the same ideas to the HER.

Beginning with identifying metal combinations, then fabricating the electrodes, testing for the best elecrocatalyst combination, characterizing this combination, and finally applying further improvements by applying the electrocatalyst to a high surface area support in order to address item 2.

5.2 Future Work

To continue the momentum and insights gained in this work the following should be addressed:

1. Can machine learning be utilized to identify likely combinations of multimetal catalysts that can surpass current noble metals?
2. How can electrolyzer design be manipulated to achieve optimal catalytic results?
3. What are alternative options for storing hydrogen?
4. To implement, how can materials cost be reduced to decrease the high capital cost of an electrolyzer start-up?

The first item is an idea to expand on the preliminary combination search conducted in this study. As another metal is added to the mix, the variables becoming exponentially more complicated to predict based on synergistic effects. If there was a way to scan many different combinations of elements in various quantities this could help to narrow down which metals in what combinations would be worth synthesizing via the microwave-assisted synthesis. The second item refers to the different ways in which the electrolyzer can be designed. For example how many electrodes to include within a device and if they should be in series or parallel. The last two future work items regard the whole process, outside of catalysis, once it has been established.

References

[1] Doman, L. Alternative Fuels Data Center. https://www.eia.gov/todayinenergy/detail.php?id=32912.

[2] Moon, B. K. Secretary-General's remarks at event on "Clean Industrial Revolution". https://www.un.org/sg/en/content/sg/statement/2011-12-06/secretary-generals-remarks-event-clean-industrial-revolution.

[3] Lüthi, D.; Le Floch, M.; Bereiter, B.; Blunier, T.; Barnola, J.-M.; Siegenthaler, U.; Raynaud, D.; Jouzel, J.; Fischer, H.; Kawamura, K.; Stocker, T. *Nature* **2008**, *453*, 379.

[4] NOAA, https://www.noaa.gov.

[5] Kasting, J. F.; Ackerman, T. P. *Science* **1986**, *234*, 1383–1385.

[6] Scholz, W. H. *Gas separation & purification* **1993**, *7*, 131–139.

[7] Edwards, P. P.; Kuznetsov, V. L.; David, W. I.; Brandon, N. P. *Energy policy* **2008**, *36*, 4356–4362.

[8] Veziro, T.; Barbir, F. *International Journal of Hydrogen Energy* **1992**, *17*, 391–404.

[9] Cammack, R.; Frey, M.; Robson, R. *Hydrogen as a fuel: learning from nature*; CRC Press, 2015.

[10] Jain, I. *International journal of hydrogen energy* **2009**, *34*, 7368–7378.

[11] Albonetti, S.; Perathoner, S.; Quadrelli, E. A. *Horizons in Sustainable Industrial Chemistry and Catalysis*; Elsevier, 2019; Vol. 178.

[12] Mishra, A.; Basu, S.; Shetti, N. P.; Reddy, K. R.; Aminabhavi, T. M. *Nanoscale Materials in Water Purification*; Elsevier, 2019; pp 759–781.

[13] Curie, M. *Renewable Hydrogen Technologies: Production, Purification, Storage, Applications and Safety* **2013**, *43*.

[14] Walter, M. G.; Warren, E. L.; McKone, J. R.; Boettcher, S. W.; Mi, Q.; Santori, E. A.; Lewis, N. S. *Chemical reviews* **2010**, *110*, 6446–6473.

[15] Gupta, R. B. *Hydrogen fuel: production, transport, and storage*; Crc Press, 2008.

[16] Horkans, J.; Shafer, M. *Journal of The Electrochemical Society* **1977**, *124*, 1202–1207.

[17] Trasatti, S. *Electrochimica Acta* **1984**, *29*, 1503–1512.

[18] Reier, T.; Oezaslan, M.; Strasser, P. *Acs Catalysis* **2012**, *2*, 1765–1772.

[19] Rossmeisl, J.; Qu, Z.-W.; Zhu, H.; Kroes, G.-J.; Nørskov, J. K. *Journal of Electroanalytical Chemistry* **2007**, *607*, 83–89.

[20] Trotochaud, L.; Ranney, J. K.; Williams, K. N.; Boettcher, S. W. *Journal of the American Chemical Society* **2012**, *134*, 17253–17261.

[21] Liu, R.; Lin, Y.; Chou, L.-Y.; Sheehan, S. W.; He, W.; Zhang, F.; Hou, H. J.; Wang, D. *Angewandte Chemie International Edition* **2011**, *50*, 499–502.

[22] Plata-Torres, M.; Torres-Huerta, A. M.; Dominguez-Crespo, M. A.; Arce-Estrada, E. M.; Ramirez-Rodriguez, C. *International Journal of Hydrogen Energy* **2007**, *32*, 4142–4152.

[23] Dau, H.; Limberg, C.; Reier, T.; Risch, M.; Roggan, S.; Strasser, P. *ChemCatChem* **2010**, *2*, 724–761.

[24] Man, I. C.; Su, H.-Y.; Calle-Vallejo, F.; Hansen, H. A.; Martínez, J. I.; Inoglu, N. G.; Kitchin, J.; Jaramillo, T. F.; Nørskov, J. K.; Rossmeisl, J. *ChemCatChem* **2011**, *3*, 1159–1165.

[25] Gong, M.; Wang, D.-Y.; Chen, C.-C.; Hwang, B.-J.; Dai, H. *Nano Research* **2016**, *9*, 28–46.

[26] Yin, S.; Tu, W.; Sheng, Y.; Du, Y.; Kraft, M.; Borgna, A.; Xu, R. *Advanced Materials* **2018**, *30*, 1705106.

[27] Louie, M. W.; Bell, A. T. *Journal of the American Chemical Society* **2013**, *135*, 12329–12337.

[28] Hunter, B. M.; Blakemore, J. D.; Deimund, M.; Gray, H. B.; Winkler, J. R.; Müller, A. M. *Journal of the American Chemical Society* **2014**, *136*, 13118–13121.

[29] Barforoush, J. M.; Jantz, D. T.; Seuferling, T. E.; Song, K. R.; Cummings, L. C.; Leonard, K. C. *Journal of Materials Chemistry A* **2017**, *5*, 11661–11670.

[30] Friebel, D.; Louie, M. W.; Bajdich, M.; Sanwald, K. E.; Cai, Y.; Wise, A. M.; Cheng, M.-J.; Sokaras, D.; Weng, T.-C.; Alonso-Mori, R. *Journal of the American Chemical Society* **2015**, *137*, 1305–1313.

[31] Bard, A. J.; Faulkner, L. R.; Leddy, J.; Zoski, C. G. *Electrochemical methods: fundamentals and applications*; wiley New York, 1980; Vol. 2.

[32] Nørskov, J. K.; Bligaard, T.; Logadottir, A.; Kitchin, J.; Chen, J. G.; Pandelov, S.; Stimming, U. *Journal of The Electrochemical Society* **2005**, *152*, J23–J26.

[33] Quaino, P.; Juarez, F.; Santos, E.; Schmickler, W. *Beilstein journal of nanotechnology* **2014**, *5*, 846–854.

[34] Bell, A. T. *Integrated Solar Fuel Generators*; 2018; pp 79–116.

[35] Bard, A. J.; Fox, M. A. *Accounts of Chemical Research* **1995**, *28*, 141–145.

[36] Gray, H. B. *Nature chemistry* **2009**, *1*, 112.

[37] Kanan, M. W.; Nocera, D. G. *Science* **2008**, *321*, 1072–1075.

[38] McCrory, C. C.; Jung, S.; Ferrer, I. M.; Chatman, S. M.; Peters, J. C.; T. F. Jaramillo, J. A. C. *Soc* **2015**, *137*, 4347–4357.

[39] Dau, H.; Limberg, C.; Reier, T.; Risch, M.; Roggan, S.; Strasser, P. *ChemCatChem* **2010**, *2*, 724–761.

[40] Corrigan, D. A. *J. Electrochem Soc* **1987**, *134*, 377–384.

[41] Trotochaud, L.; Young, S. L.; Ranney, J. K.; Boettcher, S. W. *J. Am. Chem Soc* **2014**, *136*, 6744–6753.

[42] Bau, J. A.; Luber, E. J.; Buriak, J. M. *ACS applied materials & interfaces* **2015**, *7*, 19755–19763.

[43] Guerrini, E.; Piozzini, M.; Castelli, A.; Colombo, A.; Trasatti, S. *Journal of Solid State Electrochemistry* **2008**, *12*, 363–373.

[44] Swierk, J. R.; Klaus, S.; Trotochaud, L.; Bell, A. T.; Tilley, T. D. *J. Phys C* **2015**, *119*, 19022–19029.

[45] Zhang, X.; Xu, H.; Li, X.; Li, Y.; Yang, T.; Liang, Y. *Acs Catal.* **2015**, 580–588.

[46] Hoang, T. T.; Gewirth, A. A. *Acs Catal.* **2015**, 1159–1164.

[47] Hou, Y.; Lohe, M. R.; Zhang, J.; Liu, S.; Zhuang, X.; Feng, X. *Energy Environ Sci* **2016**, *9*, 478–483.

[48] Kim, T. W.; Choi, K.-S. *Science* **2014**, 990–994.

[49] Lu, X.; Zhao, C. *Commun Nat* **2015**, *6*.

[50] Hou, Y.; Wen, Z.; Cui, S.; Feng, X.; Chen, J. *Nano Lett* **2016**, *16*, 2268–2277.

[51] Burke, M. S.; Zou, S.; Enman, L. J.; Kellon, J. E.; Gabor, C. A.; Pledger, E.; Boettcher, S. W. *Lett J. Phys* **2015**, *6*, 3737–3742.

[52] Louie, M. W.; Bell, A. T. *J. Am. Chem Soc* **2013**, *135*, 12329–12337.

[53] Klaus, S.; Cai, Y.; Louie, M. W.; Trotochaud, L.; Bell, A. T. *J. Phys C* **2015**, *119*, 7243–7254.

[54] Hunter, B. M.; Blakemore, J. D.; Deimund, M.; Gray, H. B.; Winkler, J. R.; Muller, A. M. *J. Am. Chem Soc* **2014**, *136*, 13118–13121.

[55] Trotochaud, L.; Ranney, J. K.; Williams, K. N.; Boettcher, S. W. *J. Am. Chem Soc* **2012**, *134*, 17253–17261.

[56] Gong, M.; Li, Y.; Wang, H.; Liang, Y.; Wu, J. Z.; Zhou, J.; Wang, J.; Regier, T.; Wei, F.; Dai, H. *J. Am. Chem Soc* **2013**, *135*, 8452–8455.

[57] Yu, X.; Zhang, M.; Yuan, W.; Shi, G. *J. Mater A* **2015**, *3*, 6921–6928.

[58] Long, X.; Li, J.; Xiao, S.; Yan, K.; Wang, Z.; Chen, H.; Yang, S. *Angew* **2014**, *126*, 7714–7718.

[59] Hunter, B. M.; Hieringer, W.; Winkler, J.; Gray, H. B.; Muller, A. M. *Energy Environ* **2016**, *9*, 1734.

[60] R. D. Smith, R. D. F. S. T. C. P. B., M. S. Prevot *J. Am. Chem*, 135, 11580–11586.

[61] Landon, J.; Demeter, E.; Inoglu, N.; Keturakis, C.; Wachs, I. E.; Vasic, R.; Frenkel, A. I.; Kitchin, J. R. *Acs Catalysis* **2012**, *2*, 1793–1801.

[62] Smith, R. D.; Prevot, M. S.; Fagan, R. D.; Zhang, Z.; Sedach, P. A.; Siu, M. K. J.; Trudel, S.; Berlinguette, C. P. *Science* **2013**, *60–63*.

[63] McDonald, T. D.; Bayer, C.; DeLee, A. M.; Atchison, E.; Widrig, D.; Hutchens, B.; Leonard, K. C. *J. Electrochem* **2016**, *163*.

[64] Friebel, D.; Louie, M. W.; Bajdich, M.; Sanwald, K. E.; Cai, Y.; Wise, A. M.; Cheng, M. J.; Sokaras, D.; Weng, T. C.; Alonso-Mori, R.; Davis, R. C.; Bargar, J. R.; Norskov, J. K.; Nilsson, A.; Bell, A. T. *J. Am. Chem* **2015**, *137*, 1305–1313.

[65] Park, H. S.; Leonard, K. C.; Bard, A. J. *J. Phys C* **2013**, *117*, 12093–12102.

[66] Arroyo-Curras, N.; Bard, A. J. *J. Phys C* **2015**, *119*, 8147–8154.

[67] Ahn, H. S.; Bard, A. J. *Journal of the American Chemical Society* **2015**, *137*, 612–615.

[68] Rodriıguez-Loopez, J.; ees, M. A. A.-A.; Bard, A. J. *J. Am. Chem* **2008**, *130*, 16985–16995.

[69] Ahn, H. S.; Bard, A. J. *Journal of the American Chemical Society* **2015**, *138*, 313–318.

[70] Wang, L.; Geng, J.; Wang, W.; Yuan, C.; Kuai, L.; Geng, B. *Nano Res* **2015**, *8*, 3815–3822.

[71] Morales-Guio, C. G.; Mayer, M. T.; Yella, A.; Tilley, S. D.; Gratzel, M.; Hu, X. **2015**, *137*, 9927– 9936.

[72] Smith, R. D.; Berlinguette, C. P. *J. Am. Chem* **2016**, *138*, 1561–1567.

[73] Bergmann, A.; Martinez-Moreno, E.; Teschner, D.; Chernev, P.; Gliech, M.; de Araujo, J. F.; Reier, T.; Dau, H.; Strasser, P. *Commun Nat* **2015**, *6*.

[74] Ullman, A. M.; Brodsky, C. N.; Li, N.; Zheng, S.-L.; Nocera, D. G. **2016**, *138*, 4229–4236.

[75] Kanan, M. W.; Surendranath, Y.; Nocera, D. G. *Soc. Rev* **2009**, *38*, 109–114.

[76] Li, W.; Sheehan, S. W.; He, D.; He, Y.; Yao, X.; Grimm, R. L.; Brudvig, G. W.; Wang, D. *Angew* **2015**, *127*, 11590–11594.

[77] Blakemore, J. D.; Schley, N. D.; Olack, G. W.; Incarvito, C. D.; Brudvig, G. W.; Crabtree, R. H. *Sci* **2011**, *2*, 94–98.

[78] Masa, J.; Weide, P.; Peeters, D.; Sinev, I.; Xia, W.; Sun, Z.; Somsen, C.; Muhler, M.; Schuhmann, W. *Adv Energy Mater* **2016**, *6*.

[79] Dahal, N.; Garcia, S.; Zhou, J.; Humphrey, S. M. *Acs Nano* **2012**, *6*, 9433–9446.

[80] Katsuki, H.; Komarneni, S. **2001**, *84*, 2313–2317.

[81] Kijima, N.; Yoshinaga, M.; Awaka, J.; Akimoto, J. *Solid State Ionics* **2011**, *192*, 293–297.

[82] Baghbanzadeh, M.; Carbone, L.; Cozzoli, P. D.; Kappe, C. O. *Angew* **2011**, *50*, 11312–11359.

[83] Leonard, K. C.; Nam, K. M.; Lee, H. C.; Kang, S. H.; Park, H. S.; Bard, A. J. *J. Phys C* **2013**, *117*, 15901–15910.

[84] Machevsky, M. L.; M. A. Anderson, L. **1986**, *2*, 583–587.

[85] Atkinson, R.; Posner, A.; Quirk, J. *J. Inorg* **1968**, *30*, 2371–2381.

[86] Barforoush, J. M.; McDonald, T. D.; Desai, T. A.; Widrig, D.; Bayer, C.; Brown, M. K.; Cummings, L. C.; Leonard, K. C. *Acta Electrochim* **2016**, *190*, 713–719.

[87] Heuer, J.; Stubbins, J. *Sci* **1999**, *41*, 1231–1243.

[88] McIntyre, N.; Zetaruk, D. *Anal Chem* **1977**, *49*, 1521–1529.

[89] X-ray Photoelectron Spectroscopy Database, . *National Institute of Standards and Technology*; Gaithersburg: MD.

[90] Dresselhaus, M.; Thomas, I. *Nature* **2001**, *414*, 332.

[91] Hasanuzzaman, M.; Zubir, U. S.; Ilham, N. I.; Seng Che, H. *Wiley Interdisciplinary Reviews: Energy and Environment* **2017**, *6*, e222.

[92] Yan, K.; Sheng, M.; Sun, X.; Song, C.; Cao, Z.; Sun, Y. *ACS Applied Energy Materials* **2019**,

[93] McCrory, C. C.; Jung, S.; Ferrer, I. M.; Chatman, S. M.; Peters, J. C.; Jaramillo, T. F. *Journal of the American Chemical Society* **2015**, *137*, 4347–4357.

[94] Đukić, A.; Firak, M. *international journal of hydrogen energy* **2011**, *36*, 7799–7806.

[95] Kotowicz, J.; Jurczyk, M.; Wkcel, D.; Ogulewicz, W. *Journal of Power Technologies* **2016**, *96*, 149–156.

[96] Taylor, A. K.; Andreu, I.; Gates, B. D. *ACS Applied Energy Materials* **2018**, *1*, 1771–1782.

[97] Lyons, M.; Brandon, M. *Int. J. Electrochem. Sci* **2008**, *3*, 1463–1503.

[98] Lyons, M. E.; Brandon, M. P. *Int. J. Electrochem. Sci* **2008**, *3*, 1386–1424.

[99] Singh, R.; Pandey, J.; Anitha, K. *International journal of hydrogen energy* **1993**, *18*, 467–473.

[100] McDonald, T. D.; Bayer, C.; DeLee, A. M.; Atchison, E.; Widrig, D.; Hutchens, B.; Leonard, K. C. *Journal of The Electrochemical Society* **2016**, *163*, H359–H366.

[101] Swierk, J. R.; Klaus, S.; Trotochaud, L.; Bell, A. T.; Tilley, T. D. *The Journal of Physical Chemistry C* **2015**, *119*, 19022–19029.

[102] Barforoush, J. M.; Seuferling, T. E.; Jantz, D. T.; Song, K. R.; Leonard, K. C. *ACS Applied Energy Materials* **2018**, *1*, 1415–1423.

[103] Zhang, B.; Zheng, X.; Voznyy, O.; Comin, R.; Bajdich, M.; García-Melchor, M.; Han, L.; Xu, J.; Liu, M.; Zheng, L. *Science* **2016**, *352*, 333–337.

[104] Barr, T. L.; Seal, S. *Journal of Vacuum Science & Technology A: Vacuum, Surfaces, and Films* **1995**, *13*, 1239–1246.

[105] McIntyre, N.; Cook, M. *Analytical chemistry* **1975**, *47*, 2208–2213.

[106] McIntyre, N.; Zetaruk, D. *Analytical Chemistry* **1977**, *49*, 1521–1529.

[107] Fernandez, V. K. A.; Fernandes, D. M.; Balula, S. S.; Cunha-Silva, L.; Perez-Mendoza, M. J.; Lopez-Garzon, F. J.; Pereira, M. F. R.; Freire, C. *ACS Applied Energy Materials* **2019**,

[108] Mansour, A.; Melendres, C. *Surface Science Spectra* **1994**, *3*, 247–254.

[109] Lian, K.; Kirk, D.; Thorpe, S. *Journal of The Electrochemical Society* **1995**, *142*, 3704–3712.

[110] Temesghen, W.; Sherwood, P. *Analytical and bioanalytical chemistry* **2002**, *373*, 601–608.

[111] Hunter, B. M.; Hieringer, W.; Winkler, J.; Gray, H.; Muller, A. *Energy & Environmental Science* **2016**, *9*, 1734–1743.

[112] Tan, B. J.; Klabunde, K. J.; Sherwood, P. M. *Chemistry of Materials* **1990**, *2*, 186–191.

[113] Bard, A. J.; Faulkner, L. R. *Electrochemical Methods: Fundamentals and Applications* **2001**, *2*.

[114] Electrocatalysts, N.-I. O. O.-E. *Journal of the American Chemical Society* **2014**, *136*, 6744–6753.

[115] Batchellor, A. S.; Boettcher, S. W. *ACS Catalysis* **2015**, *5*, 6680–6689.

[116] Weber, M. F.; Dignam, M. J. *Journal of The Electrochemical Society* **1984**, *131*, 1258–1265.

[117] Goyal, R.; Minocha, A.; Singhal, S. **1986**,

[118] Murthy, A. P.; Theerthagiri, J.; Madhavan, J. *ACS Applied Energy Materials* **2018**, *1*, 1512–1521.

[119] of Energy, U. D. EIA projects 28% increase in world energy use by 2040. https://afdc.energy.gov/fuels/hydrogen.html.

[120] Voiry, D.; Yamaguchi, H.; Li, J.; Silva, R.; Alves, D. C.; Fujita, T.; Chen, M.; Asefa, T.; Shenoy, V. B.; Eda, G. *Nature materials* **2013**, *12*, 850.

[121] Zhang, H.; Li, Y.; Zhang, G.; Xu, T.; Wan, P.; Sun, X. *Journal of Materials Chemistry A* **2015**, *3*, 6306–6310.

[122] Li, Y.; Wang, H.; Xie, L.; Liang, Y.; Hong, G.; Dai, H. *Journal of the American Chemical Society* **2011**, *133*, 7296–7299.

[123] Benck, J. D.; Chen, Z.; Kuritzky, L. Y.; Forman, A. J.; Jaramillo, T. F. *Acs Catalysis* **2012**, *2*, 1916–1923.

[124] Popczun, E. J.; Read, C. G.; Roske, C. W.; Lewis, N. S.; Schaak, R. E. *Angewandte Chemie International Edition* **2014**, *53*, 5427–5430.

[125] Dupin, J.-C.; Gonbeau, D.; Vinatier, P.; Levasseur, A. *Physical Chemistry Chemical Physics* **2000**, *2*, 1319–1324.

[126] Meza, E.; Ortiz, J.; Ruíz-León, D.; Marco, J.; Gautier, J. *Materials Letters* **2012**, *70*, 189–192.

[127] Chen, Y.-W. D.; Noufi, R. N. *Journal of the Electrochemical Society* **1984**, *131*, 731–735.

[128] Biesinger, M. C.; Payne, B. P.; Grosvenor, A. P.; Lau, L. W.; Gerson, A. R.; Smart, R. S. C. *Applied Surface Science* **2011**, *257*, 2717–2730.